2019

Liquid water droplet dynamics in a PEM fuel cell channel exposed to acoustic vibrations

Preston Ryan Stolberg

Recommended Citation

Stolberg, Preston Ryan, "Liquid water droplet dynamics in a PEM fuel cell channel exposed to acoustic vibrations" (2019). *Master's Theses - College of Engineering*. 19.
https://digitalcommons.law.wne.edu/coetheses/19

Liquid Water Droplet Dynamics in a PEM Fuel Cell Channel Exposed to Acoustic Vibrations

Submitted by

Preston Ryan Stolberg

A thesis/project submitted to the Faculty of
Western New England University
in partial fulfillment of the
requirements for the Master of Science
in Mechanical Engineering

Springfield, MA
[Insert date of graduation, e.g., May 19, 2018]

Approved by

Dr. Anthony Santamaria, [academic title]	[date]
Dr. Mehdi Mortazavi, [academic title]	[date]
Dr. Jingru Benner, [academic title]	[date]
Dr. Christian Salmon, [academic title]	[date]
Dean, College of Engineering	[date]

Abstract

The goal of the thesis research outlined herein was to examine the effects of superimposing an acoustic pressure wave on air flow for the purpose of liquid water removal in a PEM fuel cell in an ex-situ test environment. An acoustic speaker was attached to the air line and a frequency was emitted from the speaker in order to integrate the wave into the air flow. Five different frequencies were tested and compared against each other and a constant of 0 Hz. Adding 80 Hz of frequency to the air flow proved to improve the rate of water removal the most at a decrease of 19.8%.

A four-piece test section was fabricated out of a clear 0.29" thick piece of polycarbonate. The test section consisted of two inlets, one outlet, and two pressure ports that allowed for conduction of the research. One is used for the injection of air, while the second inlet is used for the injection of water. The outlet is used as an exit for water and air. Finally, the two pressure ports were used for the collection of all the pressure data for the experiment.

A test setup was also constructed for the purpose of leveling the high-speed camera with the test section as well as keeping the many working materials as compact and organized as possible. The stand was created using a Ti 8020 erector set. Two separate brackets were constructed: one for the test section, and one for the high-speed camera. The test section was connected to a compressed air tank with a regulator to ensure that the desired velocity of air flow was being inputted into the cell. Additionally, a syringe pump was connected to the section that could also adjust to the desired input rate of water. Finally, two different computers connected to

the setup: one used for pressure data acquisition, and one used to control the high-speed camera and save the pictures taken.

Two separate tests were conducted throughout the entirety of this project. One test was to ensure that the test section was airtight, while the second test was the main experiment that would fulfill the goal and understanding of the project. The first experiment consisted of running the air through the test cell at different speeds while recording the pressure measurements. After the data was recorded, theoretical and tested friction factors were calculated and compared. Once the results were confirmed, it was deemed that the test section was airtight, and the main experiment could commence. The main experiment consisted of injecting air and water into the test section simultaneously to grow and detach liquid water droplets. A high-speed camera captured the growth and detachment of several droplets. Pressure data was being recorded throughout this entire process as well. All this data could be synchronized to ensure that each data point had a corresponding image.

After the data was collected, a few different statistics were made based on the pressure data, while the photographic data was used to collect data on the angles of contact. The pressure data could be used for statistics including time to detachment, maximum two-phase pressure, and droplet volume at detachment. These different statistics allowed for a basis of comparison between all the frequencies and with the constant. Additionally, the pictures were uploaded into AutoCAD so that advancing and receding contact angles could be analyzed. It was found that, for all the different statistics gathered the same trendline occurred with 80 Hz being the most effective frequency for water removal.

Acknowledgments

There are many individuals I would like to thank and credit for their ongoing support throughout the entire research process.

First, I would like to thank my co-Committee Chairs Drs. Anthony Santamaria and Mehdi Mortazavi for providing me the tools, advice and consistent support in and out of the lab. Through my Introduction to Fuel Cells class, Dr. Santamaria ignited my interest in this field. Additionally, he was able to always provide any help to any questions that I had throughout the entire process, which included trouble shooting problems, and helping me through the data analysis process. I also cannot thank Dr. Mortazavi enough for his continuous support from start to finish of this research project. He provided me with all the necessary equipment needed to perform the tasks required for this project. Additionally, he was able to guide me through the procedure of using the equipment for the purpose of data collection and image processing. Whether it was providing me with the proper equations or supplying all the papers I used in literature review, he would always have anything I needed throughout the process. I also would like to thank both individuals for the timeliness of their support. I realize that both Drs. Santamaria and Mortazavi have busy schedules, and I would ask them both for help many times a week; there was never an instance where they would not respond to any questions I had within a day or so. Additionally, they were always available for in-person conversations. Thank you both so much for your support.

I would also like to thank Drs. Salmon and Benner for being my committee members. It is an honor and a privilege to be able to present my work and findings to the both of you. Dr. Salmon has been my professor for all my Engineering Management class requirements, which allowed us to grow closer over the past year and a half. Dr. Benner was able to assist me with the set up the pressure transducer for this project, which allowed for data collection for this lab.

Next, I would like to thank Peter Bennett, the machinist on campus at Western New England University (WNEU). His machining of the four different pieces that comprised the test section were critical to the to the success of this project. Without him, this project would not be possible.

I would also like to thank Cory Arden and Joseph Conners for their help and support. As a part of their senior design projects, they were tasked with helping me speed up the process of creating and submitting CAD drawings to Mr. Bennett so that I could have a test section to work with. Additionally, they also helped me set up the test stand that was used throughout the process. This was challenging because the camera needed to be in perfect line with the test section, and both Cory and Joe were integral in making this possible.

I would like to next thank Dannielle Croft, the Mechanical Engineering Lab Supervisor at WNEU. She was imperative to getting any extra materials. Dannielle was the main contact point for any Purchase Orders required for this research project. She was also very easily accessible and was always willing to help when called upon. Additionally, she managed the scheduling for the high-speed camera, which was crucial to the data collection for this project.

Next, I would like to thank Alexander Coverdill and William Yameen for their support throughout the process. Both of these two gentlemen would help me out with any extra work I would need completed. For example, Alex helped me develop a process and procedure for synchronizing the two computer timers to ensure that the pressure points collected would coincide with the images taken. Billy helped me wire all the data acquisition components.

Additionally, I would like to thank WNEU and the College of Engineering for allowing me to pursue my Bachelors' and eventually, my Masters' degrees and for funding all my research. Without the financial support given, there is no possible way this valuable research could be conducted.

Lastly, I would like to thank my biggest support group, my family and my girlfriend. Mom, Dad, Jocelyn, PJ and Lindsey, there is no possible way I would have been able to complete this Masters' Thesis without all your love and support. Thank you for always listening and talking to me about the trials and tribulations that occurred throughout this process and pushing me to succeed in everything I have and will do.

Table of Contents

Table of Contents

List of Illustrations

List of Abbreviations

PEM	Proton Exchange Membrane
GDL	Gas Diffusion Layer
VOC	Volatile Organic Compound
kW	Kilowatt
PDMS	Polydimethylsiloxane
Pa	Pascals
RSE	Single-Ended Ground Referenced signal sources

Background

Introduction to Fuel Cells

Proton Exchange Membrane (PEM) fuel cells are becoming increasingly used throughout society today because of their ability to run at higher efficiencies and ability to run on the renewable resources, hydrogen and oxygen. Hydrogen and oxygen enter from either side of the fuel cell and are combined at the ion exchanging membrane, where water and energy are the byproducts. For these reasons, companies like Honda and Toyota are beginning to implement fuel cell run automobiles into their inventory of vehicles. Typically, these companies use batteries or internal combustion engines as a source of power generation.

The drawbacks of the conventional motor is that a battery takes a very long time to charge, the engines are typically very loud, cause a lot of vibration, and can have very high maintenance costs. Batteries are very heavy, which causes a lot of added stress on to the engine. A car battery can add up to 50 pounds to the overall weight of the car. This may not seem like a lot, but in addition to the 600 pounds that the engine and transmission weigh, it is a lot of added weight to the entire body of the automobile. This 650-pound extra load can really wear down a car over time and cause problems.

Along with the added weight of the engine and battery, conventional internal combustion engines also emit many toxic elements into the air. The fundamental emissions of gas-powered cars are: Nitrogen gas (N_2), carbon dioxide (CO_2), and water vapor (H_2O). All the main emissions do not seem too catastrophic; however, CO_2 is a large contributor to global warming. In addition to all the main emissions, there are smaller amounts of extremely harmful pollutants that are produced in the conventional engine. Carbon monoxide (CO) is an extremely poisonous gas that is colorless and odorless. This makes it extremely difficult to detect as well as its actual impact on the environment. Volatile organic compounds (VOCs) are a large portion of smog that is produced when fuel is not burned completely or properly. VOCs can cause many effects to a person's health including eye, nose and throat irritation, headaches, kidney and liver damage, and sometimes cancer. Finally, Nitrogen Oxides, a combination of NO and NO_2, contribute to the formation of smog and acid rain. This can be detrimental to people as it causes irritation to the human mucus membranes. Additionally, NO_x gases can negatively impact vegetation. It can cause leaf damage, reduced growth, and more easily impacted by diseases and frost damage. These pollutants have negative impacts on the population, as well as the environment, which, in the future, will impact the population yet again.

In 1839 Sir William Robert Grove mixed hydrogen and oxygen in the presence of an electrolyte producing water and electricity. Around 50 years later, William White Jaques coined the term "fuel cell" when he began his research using phosphoric acid in an electrolyte bath. Another 50 years passed and Francis T Bacon began researching his own methods to creating and utilizing fuel cells. He exchanged the more expensive platinum catalyst with a much less corrosive alkaline electrolyte and inexpensive nickel electrode. Bacon's research took him 27 years, but in 1959, the "Bacon Cell" was able to create 5 kW and power a welding machine.

How a Fuel Cell Works

In simplest terms, a fuel cell creates energy by a redox reaction between hydrogen and oxygen. This reaction results in the formation of water, heat and electricity. A fuel cell's composition is relatively simple in that it mirrors itself on each side and can be seen in Figure 01.

The outermost layers are the flow channels where the reactants (H_2 on the anode side, and O_2 on the cathode side) enter. Next is the gas diffusion layer (GDL) which is a hydrophobic layer that allows gas to flow toward the center and liquid to flow outward. The penultimate layer from the middle is the catalyst layer. This section of the fuel cell serves different purposes on either side: on the anode side of the cell, it allows the hydrogen to split into protons and electrons while on the cathode side it allows for oxygen reduction by reacting the protons of each side to create water. Finally, at the center of the cell, the proton exchange membrane conducts the positively charged ions that have separated to facilitate a reaction, while not allowing the negatively charged electrons to pass through. The equation that governs the entire fuel cell in terms of Hydrogen and Oxygen is as follows

$$2H_2 + O_2 \rightarrow 2H_2O + Energy \qquad \text{Eq. 1}$$

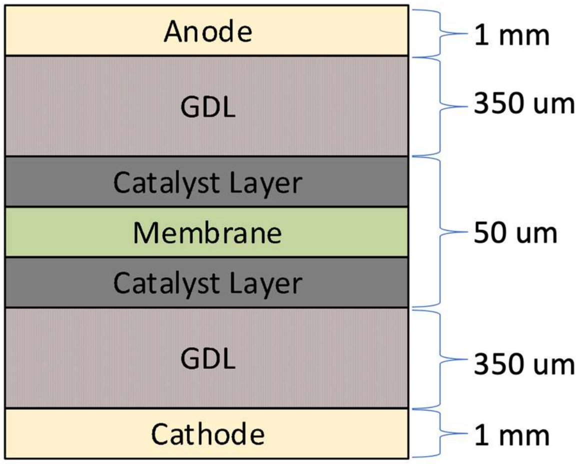

Figure 01: Fuel Cell Composition

A fuel cell's performance can be tracked through the use of a polarization curve and power density curve. This polarization curve includes a Y-axis of cell voltage (V), and an X-axis of current density (mA/cm^2). The power density curve includes a Y-axis of power density (W/cm^2)

and the same X-axis of current density used in the polarization curve. An ideal polarization and power density curve can be seen in Figure 02.

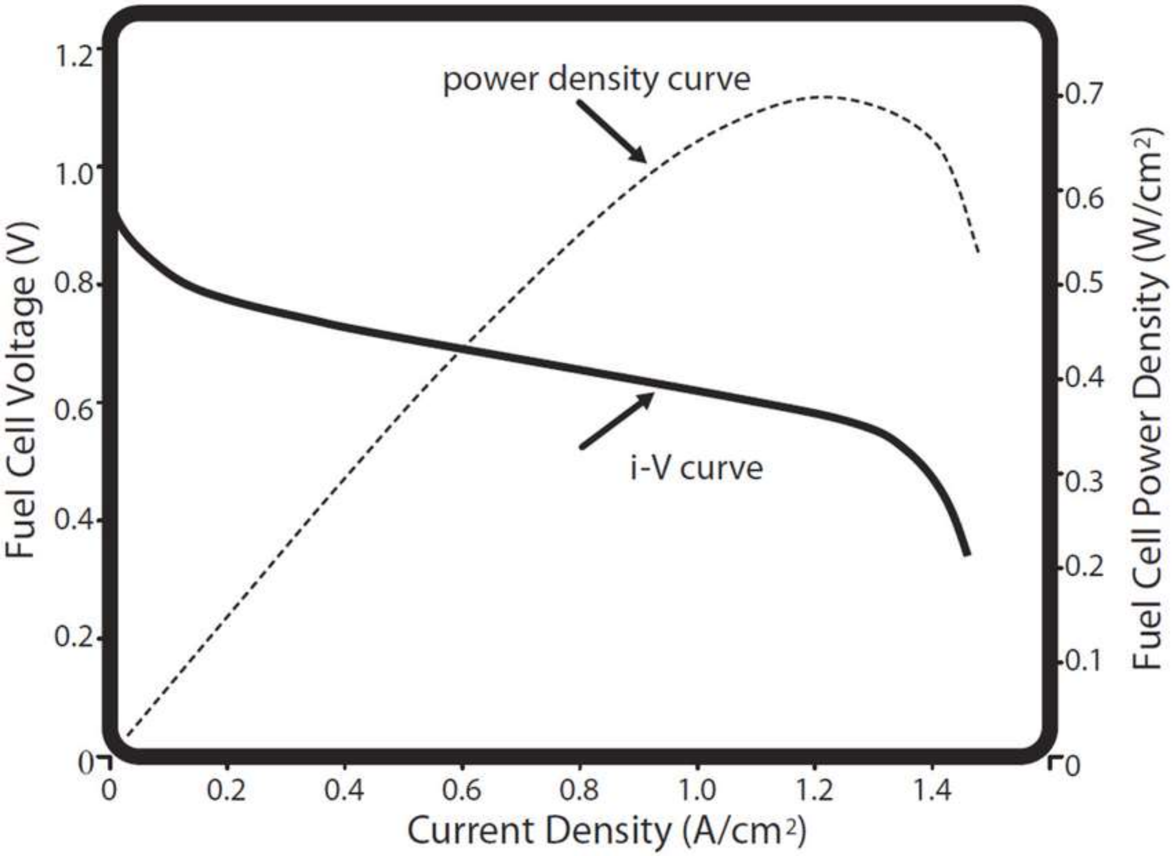

Figure 02: Theoretical Polarization Curve and Power Curve [1]

The polarization curve (solid dark line in Figure 02) is characterized by three separate regions: Activation, Ohmic, and Concentration regions. Fuel cell energy is characterized by the equation

$$E_{cell} = E - \eta_{act} - \eta_{ohm} - \eta_{conc} \qquad \text{Eq. 2}$$

Where:

E_{cell} = Total net cell energy

η_{act} = Activation losses

η_{ohm} = Ohmic losses

η_{conc} = Concentration losses

The areas most impacted by the over accumulation of water are the Ohmic and Concentration regions. The Ohmic region, which is also the longest and greatest region of loss, is governed by the equation:

$$\eta_{ohm} = j(R_{elec} + R_{ionic}) \qquad \text{Eq. 3}$$

Where:

j = Current (Amperes)

R_{elec} = Electrical resistance (bipolar plates, cell interconnects, and contacts)

R_{ionic} = Ionic resistance (resistance of the electrolyte)

The electrical resistances include the resistivity of each of the components of the fuel cell. These components include the cathode/anode bipolar plates, the GDL, and the cathode/anode catalyst layers. Not only do each of these components add resistance, but their complex interfaces also add to the resistance total. The ionic resistance portion of the equation includes resistance of the membrane. Its resistance is a large function of how much the membrane is hydrated. Along with the membrane resistivity, the ionic resistance also includes the contact between catalyst layer and the membrane. Adding extra water to this equation would mean that there is more added resistance to this section of the polarization curve, limiting the cell potential even more.

The end of the polarization curve is dominated by the diffusion and is the onset of performance instability. This region can be characterized by Equation 4 below.

$$\eta_{conc} = \frac{RT}{nF} \ln \left(\frac{C_R^o}{C_R^*}\right) \qquad \text{Eq. 4}$$

Where:

C_R^o = Bulk channel flow concentration

C_R^* = Catalyst Layer concentration

$\frac{RT}{nF}$= Gas, temperature to number of moles and Faraday's number ratio

This equation is governed by how much reactant (Hydrogen and Oxygen) is actually able to be used to form the product of H_2O. The bulk channel flow concentration of the equation refers to how much reactant is in the channels that can be used; whereas the catalyst layer concentration refers to how much of that reactant from the channels was actually able to make it passed the Catalyst Layer into the membrane for the necessary processes to take place to create energy. flooding adds loss to the Concentration region. Additionally, the diffusion of hydrogen and oxygen particles is driven by the concentration gradients. Diffusion allows each set of particles to navigate their way through the GDL to the membrane where they react together forming the byproducts. During the concentration region of the polarization curve, more hydrogen and oxygen are being diffused than during the ohmic region on the curve. The reason for this is because during the concentration region, the limiting current density at the catalyst layer is near zero (0). Fick's First Law of Diffusion is used to describe the diffusion that occurs within a fuel cell.

$$J_i = -D\frac{C_1 - C_2}{L} \qquad \text{Eq. 5}$$

Where:

J_i = Flux

D = Diffusion Constant (length / time)

C = Concentration constants

L = Length

Flooding in the channels does not allow as much Oxygen to be fed to the membrane so that the necessary reactions can take place. This not only impacts the bulk channel flow concentrations of the Concentration region, but the Catalyst Layer concentration because there is a lacking concentration of Oxygen being fed through the Catalyst Layer.

Problem Statement

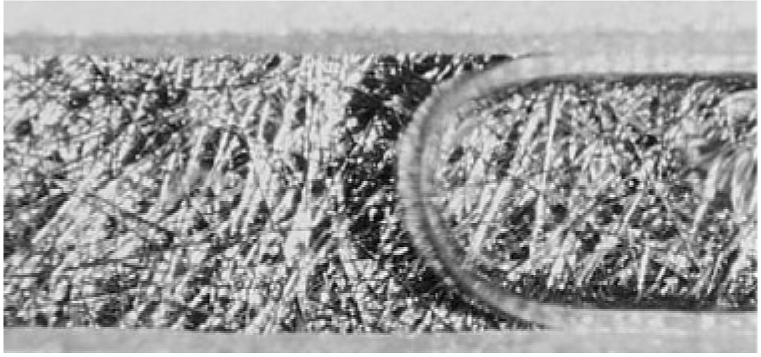

Figure 03: Fuel Cell Channel Flooding [2]

The problem that persists with PEM fuel cells is water management specifically the removal of liquid water from the cell. Although water is needed to keep the ion-conductive membrane hydrated, any excess can be detrimental to the performance of the cell. The gas diffusion layer (GDL), of the fuel cell, is one of the root causes of flooding because it allows the produced water to block its open pores and allow less reactant to travel to the catalyst layer. This water accumulation along and within the GDL pores is known as flooding and results in much lower cell performance. Moreover, GDL flooding also is cause for concern in regard to freezing, start-up conditions, and degrading over time. Taking all of this into account, finding new ways to efficiently remove water from the fuel cell is of paramount importance to the future of the technology.

Literature Review

Vibrating Surfaces

One proposed technique for removing water from the surface of a PEM fuel cell is to superimpose different types of sound waves into the surface where the droplets are situated to help the droplets release easier. Palan et al. vibrated a flexural plate with different frequencies while droplets were resting on it to induce droplet movement in the direction the waves were moving. This study found that the higher the frequency of the vibration amplitude in the surface, the smaller the radius of the droplet at detachment. However, this study also found that at higher frequencies, the droplet sizes were much smaller at release.

Another use of surface vibration was conducted by using surface acoustic waves to excite the water droplet through the material it is resting on. Palan et al. attempted to do this through the use of Rayleigh waves imposed on a surface with a pair of inter-digital transducers. This study was conducted using a steel plate as the surface material. Like the first study, this one also found that the higher the amplitude of vibration, the smaller the droplet's radius was at detachment.

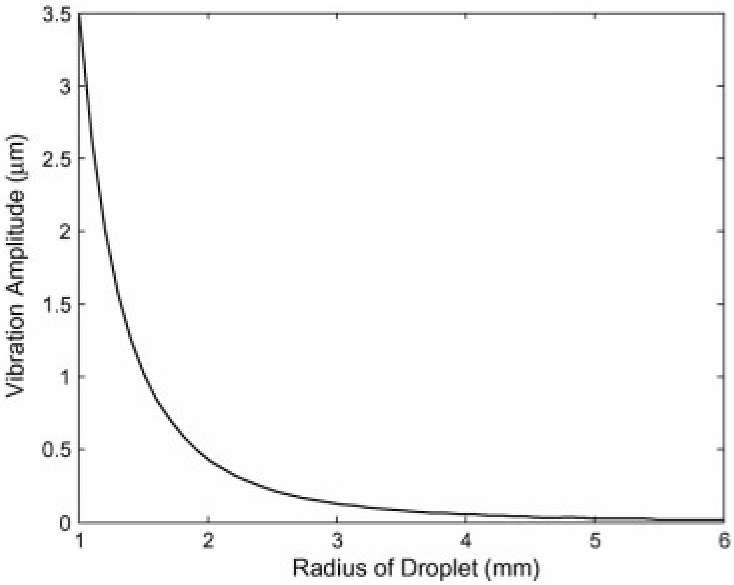

Figure 04: Result from Palan et al. Experiment [3]

Piezoelectric Actuation

A different idea presented was to move the water droplets using polystyrene particles as a slow-moving wave field. Palan et al. was able to implement this theory by placing two separate piezoelectric actuators were placed at either end of the flow channel. The actuator at the end that was in the direction of the flow had a higher excitation frequency than the actuator at the other end of the channel to cause the polystyrene particles to move slowly toward the higher frequency actuator. These actuators did not cover up the ends so that they did not interfere with gas flow or water exiting the flow field.

Droplet Angle Hysteresis

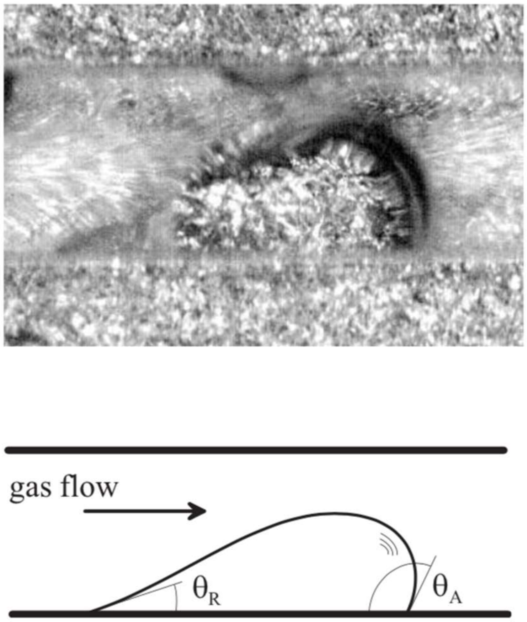

Figure 05: Example of Droplet Angle Contact [4]

It has been demonstrated that if the droplet can overcome a certain angle of contact, then it will detach from the surface. It has been hypothesized that vibrating the water droplets by superimposing acoustic vibrations into the fluid that forces the droplets to detach could cause a faster detachment. Schaeffer et al. states "If the droplet rocks between a forward moving hysteresis and one moving upstream, the contact angle hysteresis can serve to propel the fluid mass forward for a portion of the rocking motion, allowing the fluid inertia to assist in overcoming the contact line pinning holding the mass in place" [3]. To do this experiment, the gas used to propel the droplet forward was nitrogen. Along with using nitrogen, this study also involved using two different materials to situate the droplet: a 1 mm x 1 mm Plexiglas, and Polydimethylsiloxane (PDMS) flow channel. Along with both 1x1 mm square channels, the same tests were run with circular cross-sectional flow channels made entirely of PDMS. The result of this study showed that at higher flow rates of water, the effect of the flow modulation dwindles. Additionally, higher pressure drops further down the channel is required to move a higher volume of water. When the water flow rate is lower, the modulation of the flow was much more pronounced and impacted the detachment of the droplet.

Accumulation and Oscillation Studies

A similar experiment to the one being conducted in this paper was held on the campus of Western New England University. This study consisted of two separate parts to begin understanding the angle hysteresis of the droplet as well as seeing how water accumulates in the flow channels over time. The channel used for the accumulation study was similar in size to the test section being used in this experiment. Its pressure measurement length is 90 mm, while the channel dimensions are 3 mm wide, 2.4 mm tall, and 128 mm long. Different water flow rates were tested against a single air flow rate. Another similarity to the study being discussed in this paper, both studies conducted also superimposed acoustic waves into the air that was being pumped into the channel. Through this water accumulation study, Mortazavi et al. found that when an 80 Hz acoustic wave was sent through the channel, the wetted are reduced around 85% from when 0 Hz were sent through the channel. Additionally, the largest pressure drops within the cell also occurred when superimposing 80 Hz into the air supply. Figure 06 shows the relationship between cumulative water area and different superimposed frequencies. This figure displays, yet again, how 80 Hz had the largest impact on water culmination within a flow channel.

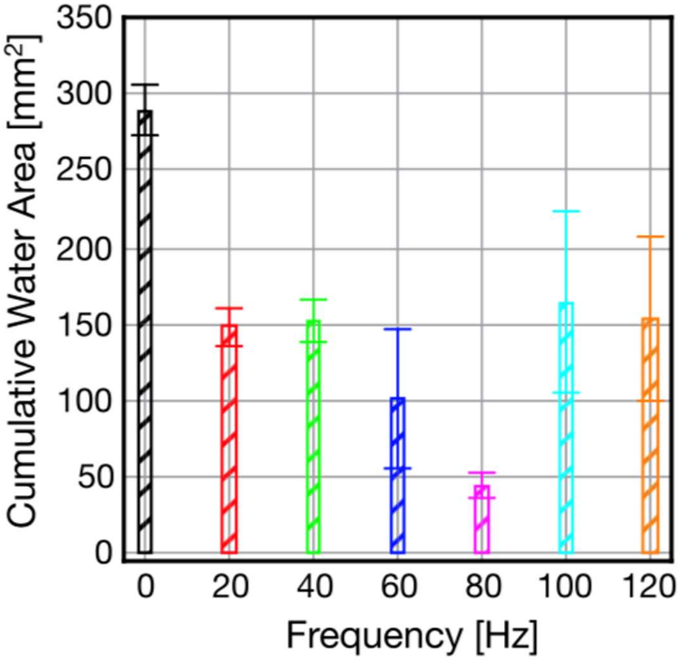

Figure 06: Cumulative Water Area vs Frequency [5]

The second half of this study consisted of attempting different speaker input configurations to identify if there was a correlation between different patterns of speaker superimposition and how fast the droplets would detach. This test utilized a different test section with smaller dimensions than the section from the first. The channel dimensions were 5 mm wide, 4.5 mm tall, and 100 mm long. Another distinction in this study was that different air flow rates were tested against a single water flow rate, while only utilizing 20 Hz as the frequency added to the air. Mortazavi et al. concluded from this study that the most energy was used by the speaker to remove the water when the speaker was on constantly, while the lowest amount of energy used was when the speaker was used on demand, when necessary. However, the lowest amount of water accumulation seemed to almost always be when the 20 Hz was pulsating on and off every ten seconds.

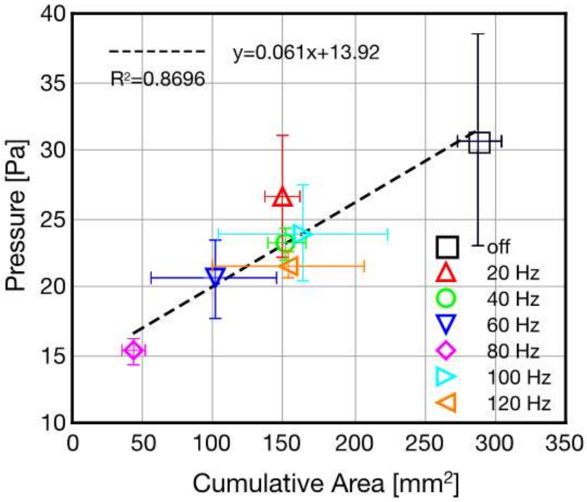

Figure 07: Pressure vs Cumulative Area [4]

Testing Apparatus

Test Section Design

All the drawings for this test section were supplied by Dr. Mehdi Mortazavi. The Solidworks model renderings of these drawings were completed by both Cory Arden and Joseph Conners. Those Solidworks drawings were then supplied to the machine shop at Western New England University and created by Peter Bennett.

The test section consisted of four separate pieces that, together, form the flow channel used for the experiment. Each piece is made of a transparent polycarbonate that allows for the visualization of the droplets as they grow and detach from the aperture hole. Figure 08 displays how each piece fits together to form the channel used. The dimensions of the channel are 3.75-mm wide, 3.6-mm tall, and 140-mm long. There are 12 holes that run outside of the channel that allow a bolt to keep the test section together. These holes do not interfere with the channel. However, only eight of the holes were used to allow for mounting of the test section on the test stand. To ensure that the GDL being used would not break, to keep the section airtight, and to preserve the polycarbonate, O-ring grooves were added to the bottom and top pieces of the test section. These grooves housed 3 separate rubber O-rings that compressed enough as to not damage the components of the test section.

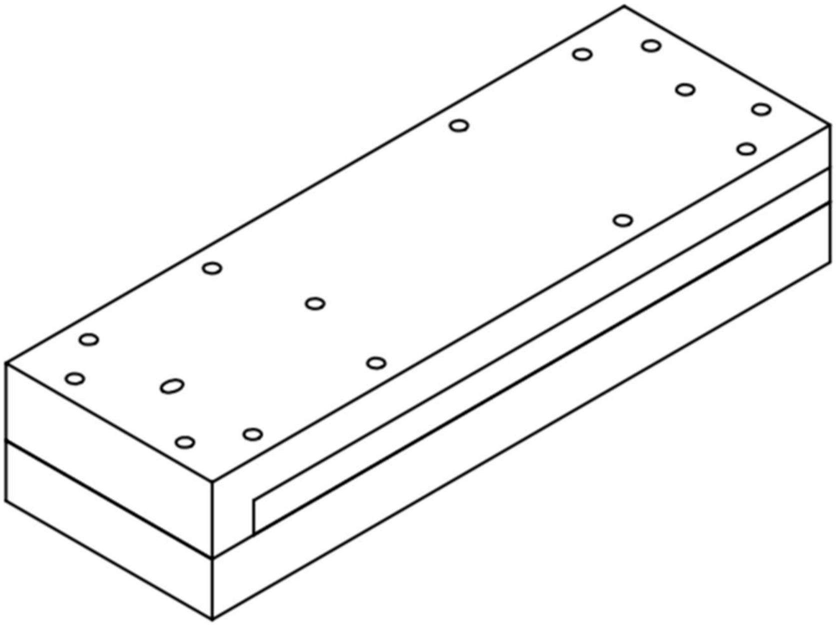

Figure 08: Assembled Test Section

The top piece of the of the test section not only creates the top wall of the flow channel, but also houses important output and input holes that allow for data collection. A 45º hole enters the topmost face of the polycarbonate plate that enters at 1/8" and exits into the flow channel at 0.08". This smaller diameter hole is to allow the 1/8" tubing to fit in the whole and not enter the channel. Additionally, the smaller diameter hole acts as a directional guide for the air flow. Along with the air inlet hole, there are two separate pressure ports that are 88.92-mm away from each other. These holes enter the top side face at 1/8" and then halfway into the plate transition to a 1/64" hole. The reason for the drastic drop in hole diameter is similar to the air inlet in that it is meant to secure the tubing that runs to the pressure transducer, as well as ensuring that it will not enter the channel and disrupt flow. Another important factor to note about the top plate is that it allows for ease of assembly of the channel with its separate tiers. There is the middle tier not only acts as the top wall of the flow channel, but also as the width of the channel. Additionally, the lowest tier connects from to the bottom piece to allow again for ease of assembly. Finally, the middle tier houses the two separate O-rings that protect the polycarbonate from any damage that could incur from direct contact.

The bottom plate not only adds a flooring to the flow channel, but it also is the piece where the water can enter. Its dimensions are 150-mm long x 50-mm wide x 16.25-mm thick. A 0.06" diameter hole is cut directly in the center of the plate and allows for the small aperture that injects water into the flow channel. This hole has 0.06" rod inserted and sealed inside of it. The 0.06" rod has a 250 μm through hole in it. This hole allows for the injection of water to the test section. Along with the water inlet, the bottom plate can also hold an O-ring that will protect the plates as well as seal up the section to keep it airtight.

Finally, there are two side panels that form the two different sides of the flow channels. These two identical plates span the length of the flow channel. Each plate has dimensions of 140-mm long x 23.4-mm wide x 7.4-mm thick. They are also the windows in which the camera can see the droplets. Each plate had to be carefully cleaned after the machining process was done so that any residue would not impact the sight of the camera. These pieces also connect to both the top and bottom plate via five separate holes that align with the bolt holes and keep the test section secured and aligned properly. Figure 09 displays the fully assembled test section from the side that the camera viewed it to show its transparency, as well as the water inlet connected to the bottom plate.

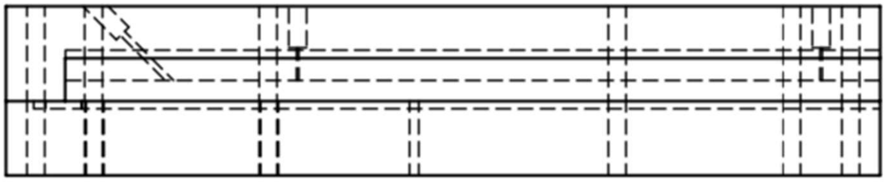

Figure 09: Side View of Fully Assembled Test Section

Experimental Setup

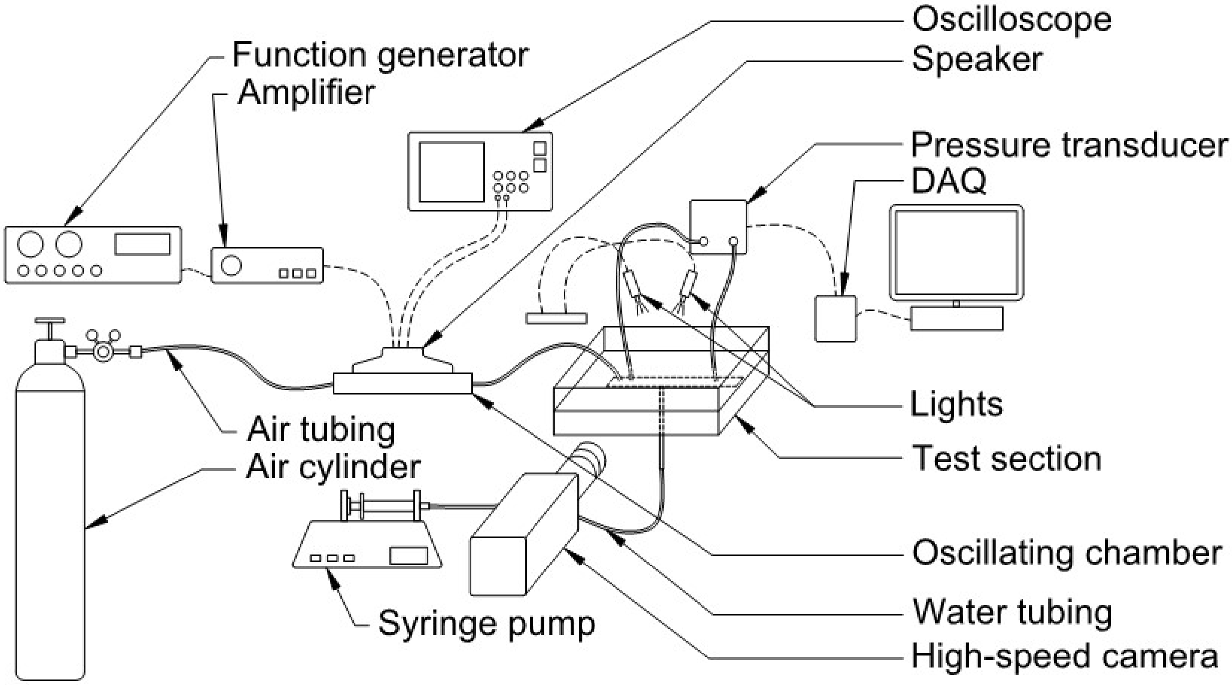

Figure 10: Schematic of Testing Setup

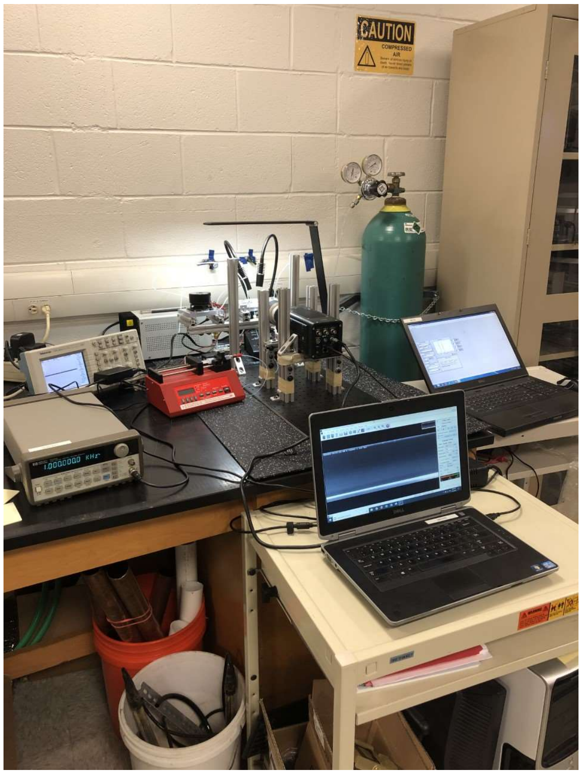

Figure 11: Entire Experimental Setup

The experimental setup for this project is set up in S109 in Sleith Hall on the campus of Western New England University. All the different items needed have a specific use that allows for ease of data collection, or test implementation. The testing setup is divided into three separate sections that all culminate in a central area where the testing and data collection all take place. These three subsections consist of the water, air and data acquisition areas. The water area only utilizes one piece of equipment, and one connection to the test section. A major component of the water section is the syringe pump. It allows for extremely slow injection rates of water into the test section. This device can inject water as slow as 1 microliter per hour, or as fast as 1000 milliliters per minute. It is very easy to control and change the rate of injection units. Along with syringe pump apparatus is the syringe that the water is dispensed. It is a rather small syringe; however a lot of water is not necessary to be pumped into the test section for this experiment.

The water passes along from the syringe pump through the tubing to the injection point that is connected to the test section. The injection point is threaded so that the connection between the syringe pump and the flow channel can be severed without cutting tubes or totally dismantling the setup. The water section of the test setup can be seen in Figure 12.

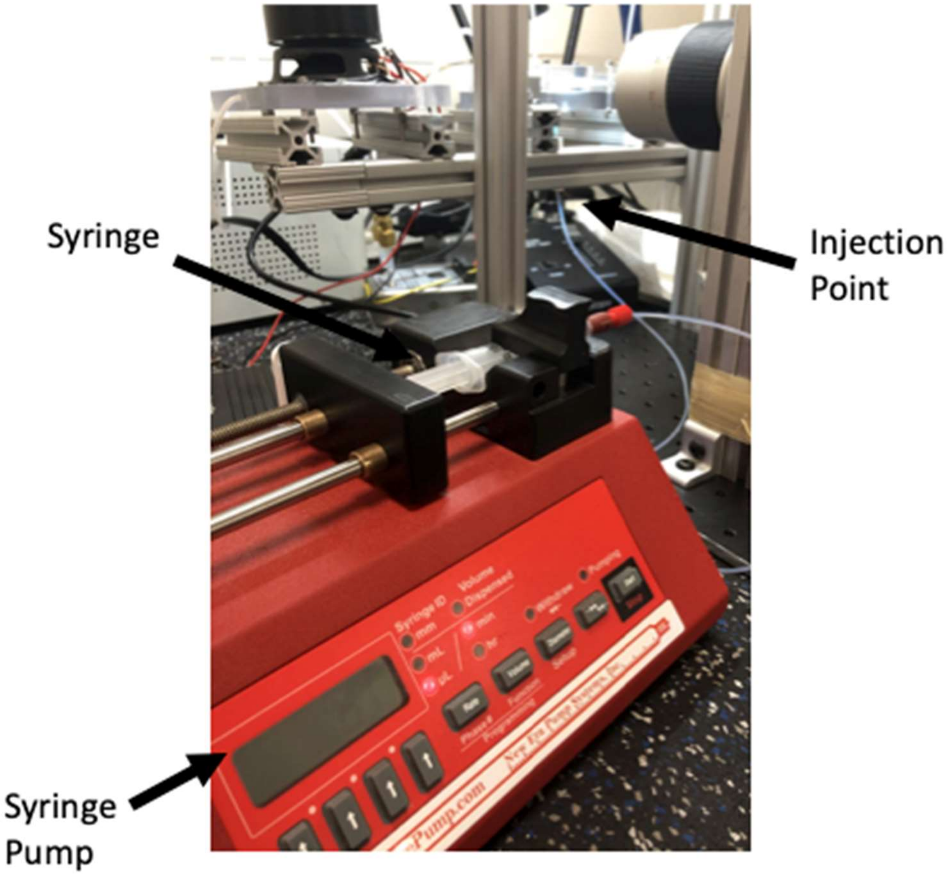

Figure 12: Water Section of the Test Setup

The next section is the group of equipment that deals with the air. This zone of equipment consists of seven different instruments that allow air to flow through the channel as well as the manipulation of that air. The first, and most important, piece in this grouping is the compressed air tank. This tank houses all the air that is used for every single test run. The cylinder connects to a regulator gage that allows the user to change the outgoing pressure of the air to speed up the air velocity or lower it. Along the tubing that connects the air to the test section are two separate valves. One of these valves is a secondary opening and closing valve. It acts as a safety measure to double secure the air when testing is completed, and the air needs to be shut off. However, it also can be used to seamlessly switch the air on and off. This valve opens and closes a lot easier than the switch that is physically attached to the compressed air cylinder. Moving on down the line is the fine-tuning knob. This piece of equipment was used for every single run throughout both procedures for this experiment. One full turn of this Swagelok knob adds about 0.00025 to the flow coefficient of air being allowed into the test section. This knob could slow or speed up the air by almost 30 mL/min to allow the flow to be as close to 6000 mL/min as possible. The next portion of the air section of the test setup allows the manipulation of air by adding acoustic waves to the airflow. First, and foremost, the 4 Ω acoustic speaker is connected directly to the air tubing. This is where the acoustic signal is transmitted to change the frequency of the air being inputted into the test section. Notice in Figure 12 that it is very close to the section, this is because if it were further away from the channel, then the frequency would dissipate over the length of the tube and not have as great of an impact on the droplet. The speaker is mounted to a polycarbonate plate and connected via four bolts around the corners of the piece of equipment. This entire assembly is connected to the test stand, situated right before the air inlet. The function generator creates the frequency that is being supplied to the air through the speaker. It adds an AM sine wave that can be changed using the knob on the right-hand side of the device. This piece of equipment is connected to the oscilloscope and the acoustic amplifier. The oscilloscope is used to monitor the output of the speaker in terms of power. It is recommended that the maximum output voltage of the speaker be no higher than 2 volts because it could cause the speaker to overheat and smoke. Controlling the output voltage of the speaker is the acoustic amplifier. This piece connects to both the oscilloscope and the speaker. The lone knob on the device controls how much voltage is being outputted. Figure 15 shows the schematic of the speaker, amplifier, function generator, and the oscilloscope. Also Figure 15 displays the wiring diagram for the speaker setup.

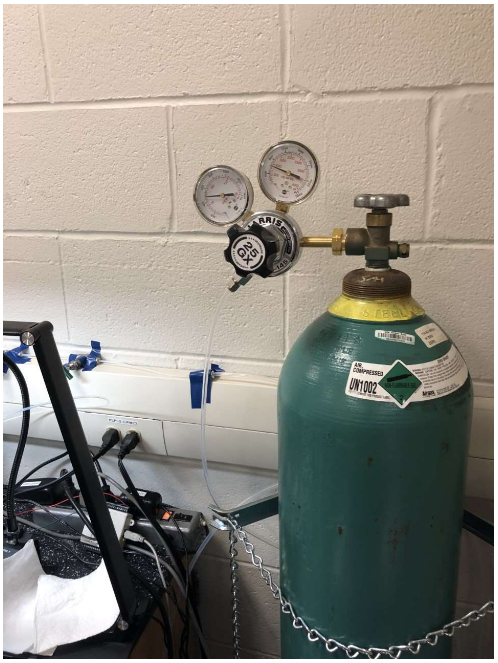

Figure 13: Compressed Air Tank and Air Regulator

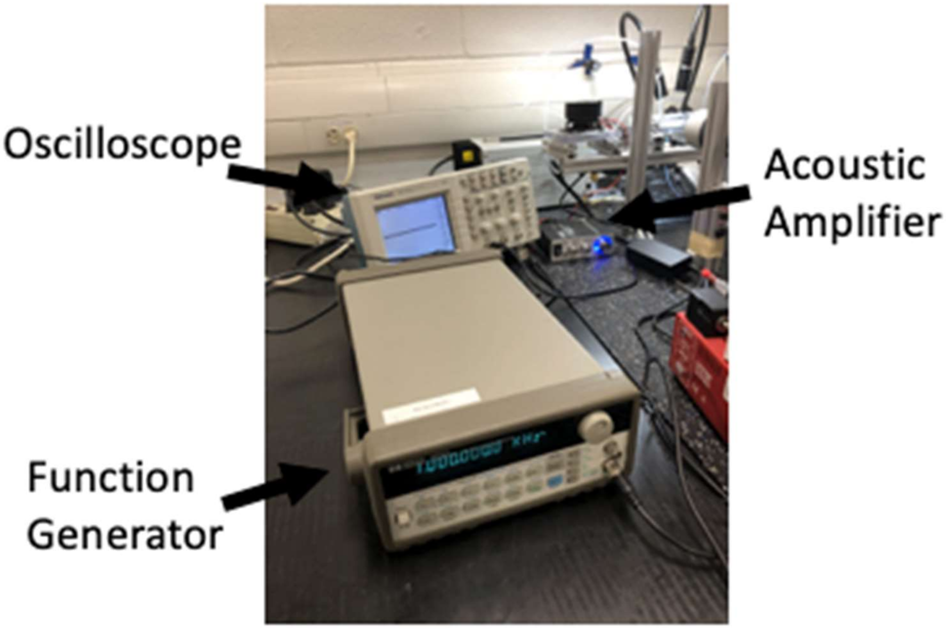

Figure 14: Function Generator, Oscilloscope, and Acoustic Amplifier

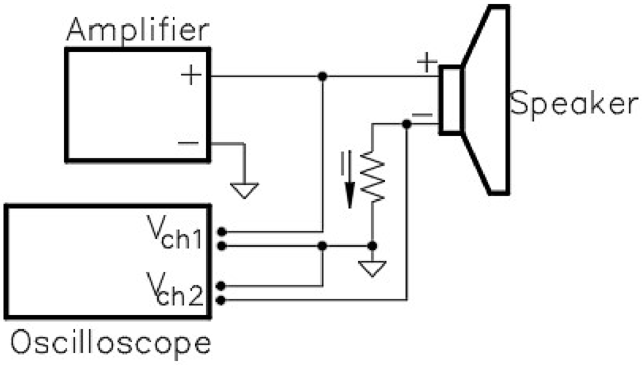

Figure 15: Wiring Diagram for Speaker Setup

The data acquisition portion of the experimental setup consists of a pressure transducer, a high-speed camera, and two separate computers that are responsible for taking in different sets of data. The pressure transducer is connected to a computer that is running LabVIEW software that reads the voltage off the pressure transducer and converts that voltage to pressure measurement in Pascals (Pa). The equation used for converting the voltage to pressure is:

$$Pressure = 31.0584 * Voltage - 31.007 \qquad \text{eq. 6}$$

Along with converting the voltage to pressure, a coinciding air flow rate can also be found. To find the correlation between flow rate and pressure, 20 data points were taken simultaneously read from the pressure transducer as well as the flow meter that was used for calibration. The conversion equation from pressure (Pa) to air flow rate (mL/min) is:

$$Flow\ Rate = 105.54 * Pressure + 331.4 \qquad \text{eq. 7}$$

The second computer is the device that controls the high-speed camera. This high-speed camera is the only source for the qualitative data taken in the entirety of this experiment. It requires its own external power source to be used. In the scope of this project, the frame rate for this camera goes up to 300 frames per second. This is to allow for the visualization of the vibrating water droplets when a frequency is superimposed on the air used to force droplet detachment. Additionally, this camera allows for the clear visualization of the droplet contact angles with the floor of the flow channel. The camera sits on the experiment stand that aligns the camera lens with the section of the flow channel where the droplets grow and detach. Each picture was saved in a folder on the desktop of the computer, and then copied to a flash drive where it was then transferred to the shared Y drive in S102. The range of images taken per test was from 6000 to 9000, which, based on the frame rate, equated to 30 seconds of photographs being taken. The entire test setup can be seen in Figure 11.

All the pieces culminate at the center in the fourth section of the test setup: the test stand. This test stand is constructed of 80/20 Aluminum Erector Set pieces. To keep the entire stand secure to the table, it was screwed into a base plate that is compatible with the screws that fit the slots in the erector set. There are 15 T-slot framing extrusions, 14 corner brackets, and 4 extended corner brackets that makeup the composition of this test stand. Additionally, 4 T-brackets had to be fabricated to join together the vertically standing and horizontally suspended support beams for the camera as a safety precaution for its weight. An extension was also added to the horizontally suspended support beam that holds the test section to accommodate the room needed for the acoustic speaker. Along with the support beams, two different sets of adjustable LED lights illuminate the test section to assure that the pictures being taken by the camera are clear and well lit. Finally, a voltage source is used as the excitation for the pressure transducer.

Methods and Procedures

Computer Software

Two different sets of computer software were used for this experiment and each software was utilized on a different computer. A couple of LabVIEW VI's were developed for this set of experiments to run. The first LabVIEW VI was created for and used during the calibration portion of the project. A National Instruments LabVIEW example VI called "Voltage – Continuous Input" was used and manipulated to suit the needs of this portion of the project. This example VI was a great template to begin forming the final VI that would be used during the main phase of testing of the experiments. A second waveform graph was added and fed by the decimate array function that was added to the block diagram. One of the waveform graphs displayed the data read by the pressure transducer, while the other waveform graph displayed the data read from the flow meter. Within the block diagrams are the conversion equations from volts to either Pascals or to mL/min.

It is also worth noting that both the pressure transducer and the flow meter were connected to and feeding information to the same NI DAQ board. To accommodate the configurations, maximum and minimum voltages of both the flow meter and pressure transducer, as well as the terminal configuration of each acquisition device, some minor modifications needed to be made to the "Channel Settings" tab in the VI. The "Physical Channel" setting is actually a text box that allows for written commands. To read from multiple channels at once, the command written was "Dev1/ai0,Dev1/ai1." Both acquisition devices utilized the same maximum and minimum output voltages, so the "Max Voltage" tab was set to 5, while the "Min Voltage" was set to 0. Finally, under the "Terminal Configuration" tab was multiple different options. The configuration for this set of data acquisition systems were both Single-Ended Ground Referenced signal sources (RSE). An RSE sourced signal means that both the input and the ground come from the same device. Both the pressure transducer and flow meter were connected to the same device, so they utilized the same ground. This VI allowed for the conduction of two separate calibration exercises that were vital to the progression of this lab into its final stages. The first being the tests run to ensure that the test section was properly sealed, and the second to create a relationship between pressure and air flow velocity.

After conducting the two calibration tests, a new VI needed to be created based on the "Voltage – Continuous Input" example. This VI code ended up being a little simpler than the first one because it only required one input. After a few trials conducted where water was injected, it was noted that the air flow was not fast enough to cause detachment. Seeing as the maximum velocity that the flow meter can read is 2000 mL/min, it was necessary to find a way to input higher air flow velocities. It was decided to take different velocities using the flow meter and correlating pressures with the pressure transducer to create a plot that converts pressure to flow rate. This conversion formula was then added to the VI to convert the pressure recorded into an air flow rate velocity. To ensure that the all the data was recorded properly, a “Write to Measurement File” block was added to the block diagram. This allowed all the data taken to be written to a Microsoft Excel file. The “Timing Settings” tab in the user interface needed to be adjusted to take a sample every 0.005 seconds. This was able to be achieved by changing the “Sample Rate” and “Number of Samples” to 200. Since the pressure can change at an instant, a sample every 0.005 seconds is necessary to ensure that the all the necessary data is being collected. This LabVIEW VI was used to then finish out the remainder of the project because it was able to take adequate amounts of data, while converting the pressure data to flow rate. The user interface of the LabVIEW VI can be seen in Figure 16.

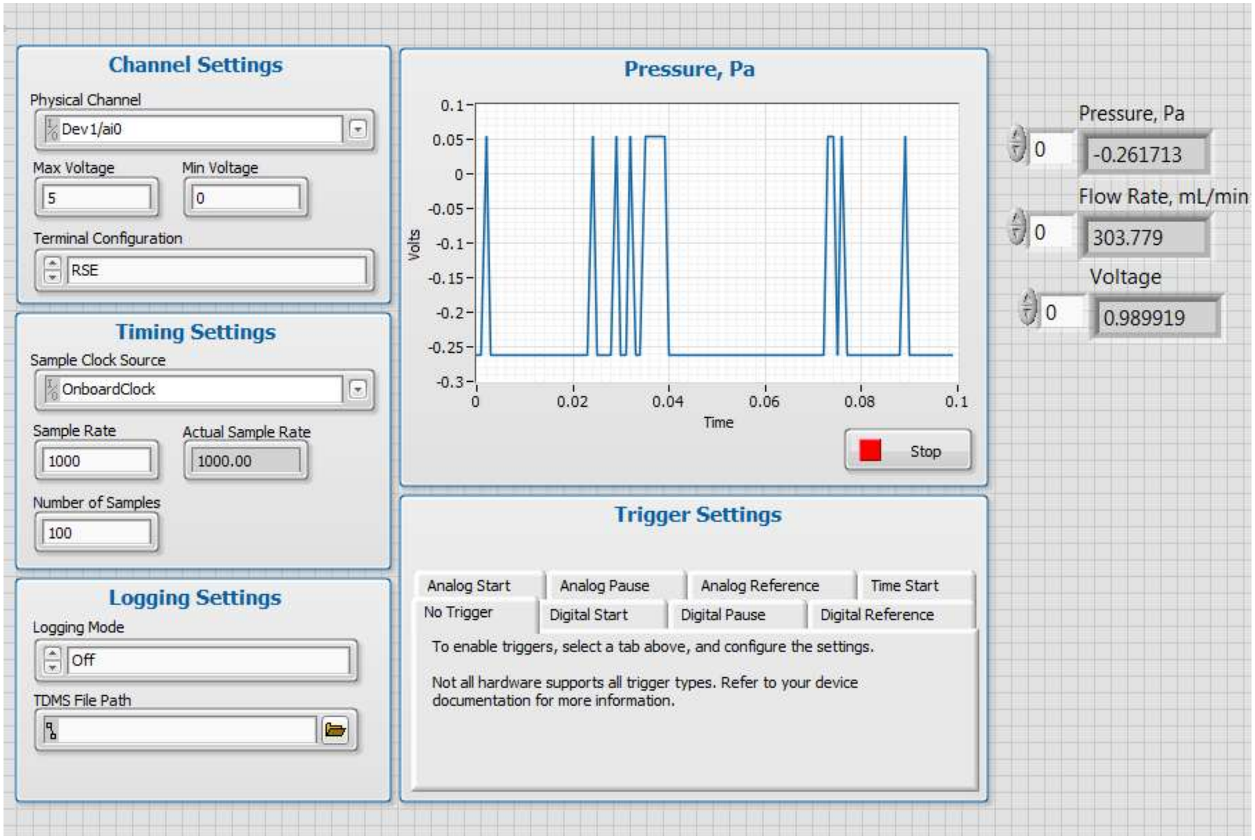

Channel Settings

Physical Channel: Dev1/ai0

Max Voltage: 5

Min Voltage: 0

Terminal Configuration: RSE

Timing Settings

Sample Clock Source: OnboardClock

Sample Rate: 1000

Actual Sample Rate: 1000.00

Number of Samples: 100

Logging Settings

Logging Mode: Off

TDMS File Path:

Pressure, Pa: 0 -0.261713

Flow Rate, mL/min: 0 303.779

Voltage: 0 0.989919

Trigger Settings

To enable triggers, select a tab above, and configure the settings.

Not all hardware supports all trigger types. Refer to your device documentation for more information.

Figure 16: LabVIEW VI Used

Along with using the high-speed camera came an entirely separate computer with an entirely separate software. The MotionPro Y4 Camera comes with a computer software that is totally compatible and allows full control of the output of the camera. It connects to the software via USB. The Motion Studio application gives the ability to change the frame rate, the exposure, the area of interest, as well as how many frames will be taken resulting in the duration of the capture. Although, there was no zoom in and out feature on this particular camera or software, it is extremely powerful and takes very detailed images. The "Play" button at the top of the right-hand side allows for a live look at what the camera sees. This gave the ability to align the camera with the flow channel and make any necessary changes that were needed before a recording would be taken. The frame rate was adjusted the most within this application because different acoustic frequencies needed different frame rates to be able to clearly see the droplet vibrations. Next, the exposure would be changed to adjust the brightness of the image. The higher the exposure, the brighter the image would be. Another useful tool embedded within this software is the storage bar at the bottom of the right-hand side. This showed how much space the images would take up with the end being the maximum number of images the camera could take in one recording. The Motion Studio application also gives the ability to adjust the different outputs of the time stamp. For this experiment, the image number, the time down to the second, the seconds after the trigger, and frame rate were all outputted. Each of these elements to the time stamp serve very distinct purposes and give vital information. Most notably, the time and time after trigger stamps. It is important to ensure the pictures taken matchup with the qualitative data taken from the Excel file. For this reason, the time stamp and time after trigger would matchup with time stamp that is printed on the Excel spreadsheet. This way, each data point has a picture to go along with it. Likewise, it is important to know the picture number so that it can be referenced later. Finally, knowing the frame rate on the pictures is important information that can be referenced in the future. Figure 17 shows all the different options discussed above. After all the camera options were set, it was then necessary to adjust the frames being taken. This was done by selecting the “Record” tab and adjusting the frames. The number of frames was the only adjustable setting on this tab, but once it was adjusted, the time of the recording session would be reflected next to it. This tab can be seen in Figure 18.

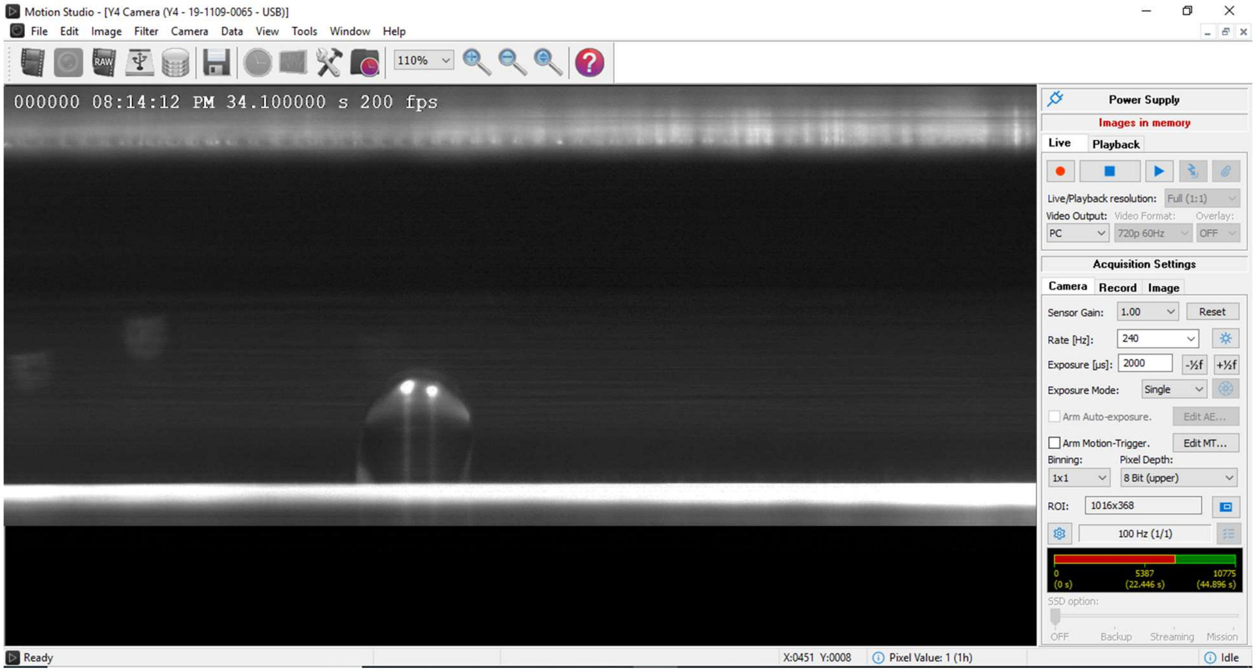

Motion Studio - [Y4 Camera (Y4 - 19-1109-0065 - USB)]

000000 08:14:12 PM 34.100000 s 200 fps

Live/Playback resolution: Full (1:1)

Video Output: PC

Video Format: 720p 60Hz

Overlay: OFF

Sensor Gain: 1.00

Rate [Hz]: 240

Exposure [µs]: 2000

Exposure Mode: Single

☐ Arm Auto-exposure.

☐ Arm Motion-Trigger.

Binning: 1x1

Pixel Depth: 8 Bit (upper)

ROI: 1016x368

100 Hz (1/1)

0 (0 s) 5387 (22.446 s) 10775 (44.896 s)

SSD option: OFF

X:0451 Y:0008

Pixel Value: 1 (1h)

Figure 17: Motion Studio Camera Options

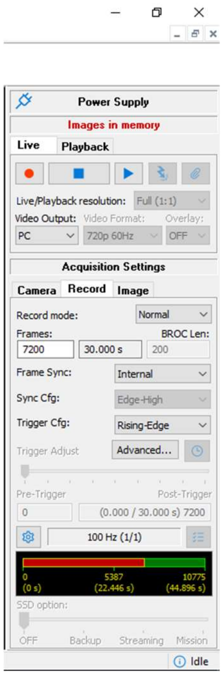

Live/Playback resolution: Full (1:1)
Video Output: PC
Video Format: 720p 60Hz
Overlay: OFF
Record mode: Normal
Frames: 7200 30.000 s
BROC Len: 200
Frame Sync: Internal
Sync Cfg: Edge-High
Trigger Cfg: Rising-Edge
Trigger Adjust
0 (0.000 / 30.000 s) 7200
100 Hz (1/1)

Figure 18: Record Tab on Motion Studio

The synchronization of both the LabVIEW and MotionPro software was also a major point of emphasis when testing began. Seeing as both were on separate computers, there were times where the local clocks on each system were telling different time. Since knowing the time down to the thousandth of a second was imperative, adjusting each clock to show the same time was done every day. To do this, the date and time settings menu on each Windows computer was brought up. Next, in the internet time panel, the "Change Settings" button was selected, bringing forward a popup. This popup would allow the synchronization of clocks with the Windows internet server time. Ensuring this procedure was done every day allowed for the most accurate synchronization of clocks. Since each photo taken prints a time stamp in the top left corner, and the LabVIEW prints all the data with a time stamp to an Excel spreadsheet, this allows the visualization of each data set by seeing a picture corresponding to a pressure measurement.

Operating Conditions

In order to be certain that the proper conditions were being run in an ex-situ lab environment, the air and water flow rates needed to be tailored to providing the best picture possible for the high-speed camera. The ideal picture set would include at least two separate droplets growing from nothing to detachment, as well as a clear view of the contact angles from the droplet to the floor of the flow channel. After multiple iterations of examining the droplets through the live feedback on the camera, it was settled that the best quality picture can occur when the air flow rate is at/or near 6000 mL/min, and the water flow rate is 60 μL/min (1μL/sec). Once this was agreed upon by all parties involved in the matter, it was time to move forward examining the different surfaces the water will flow down.

This project required the use of two separate surfaces to for basis of comparison. The first being the bare polycarbonate flooring. Polycarbonate does not have any hydrophobic properties, but the water did not have any problems traversing the surface with the aid of the air and acoustic waves. It was still possible to visualize the contact angles and take detailed pictures even with the use of the polycarbonate surface.

The high-speed camera also needed to operate at certain conditions to allow for the proper visualization of the droplet vibration. For trials that did not involve a GDL, all the frame rates for each set were 240 frames per second. At 7200 frames, this allowed for 30 seconds of images and an adequate amount that can coincide with the quantitative data points taken simultaneously

Friction Factor Test

To ensure that the test section was sealed properly, pressure and air flow rate data were both collected from a LabView code that could read these voltages simultaneously from each respective transducer. The friction factor was then calculated based on the collected today. Confirmation that the section was sealed off would result in a plot that was linear, as in the Laminar Flow section on the Moody Chart. All these calculations follow the equations that govern the Moody Chart that describes the relationship between friction and Reynold's Number in regard to flow.

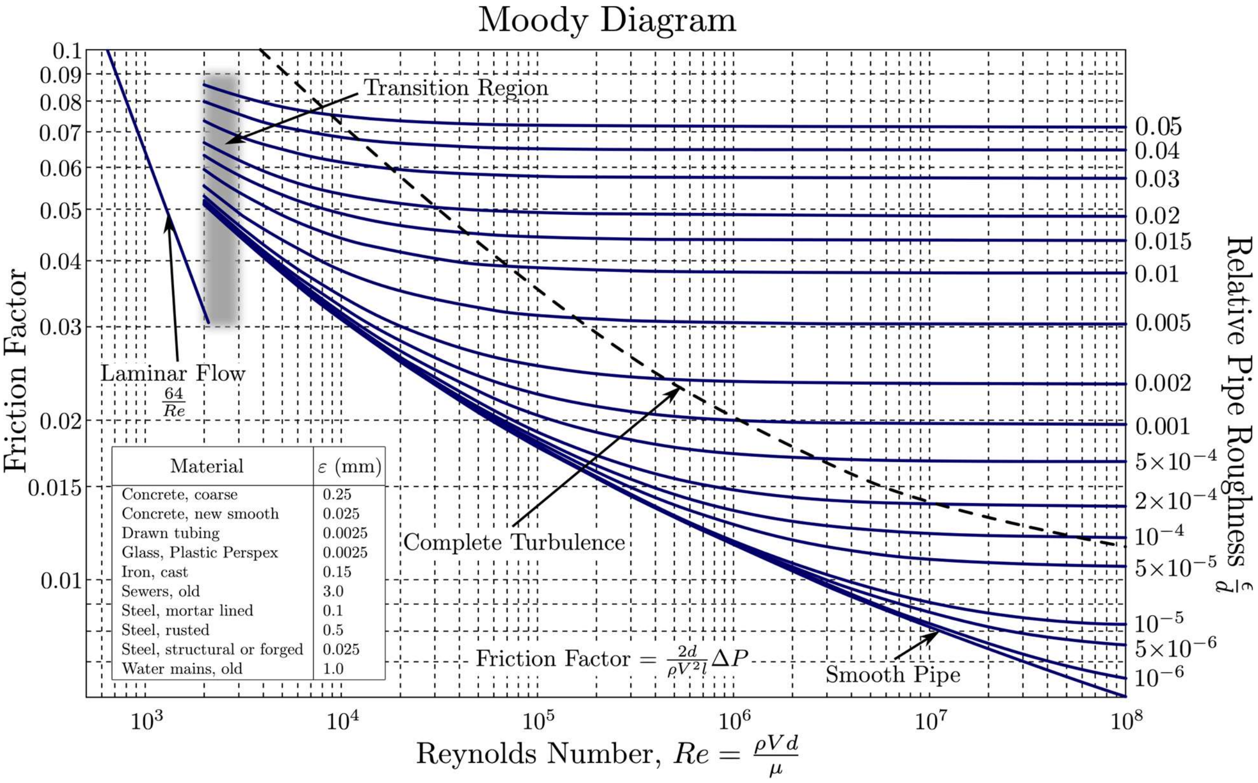

Material	ε (mm)
Concrete, coarse	0.25
Concrete, new smooth	0.025
Drawn tubing	0.0025
Glass, Plastic Perspex	0.0025
Iron, cast	0.15
Sewers, old	3.0
Steel, mortar lined	0.1
Steel, rusted	0.5
Steel, structural or forged	0.025
Water mains, old	1.0

Figure 19: Moody Chart

Equations 7, 8, and 9 were all used to find the experimental values for air velocity, Reynolds number, and friction factor, respectively. These quantities were all necessary for comparing the theoretical and experimental values of friction factor, assuring that the test section was airtight. Converting from mL/min to m^3/s only required the division of the flow rate by 60000000.

$$V = \frac{\dot{v}}{A} \qquad \text{Eq. 8}$$

Where:

V = Air Velocity (m/s)

$\dot{v}$ = Volumetric Flow Rate (m^3/s)

A = Cross-sectional Area of the Flow Channel (m^2)

Equation 8 describes the method for finding the Reynold's number which was then used to find the theoretical friction factor used for comparison.

$$Re = \frac{\rho V D}{\mu} \qquad \text{Eq. 9}$$

Where:

Re = Reynold's Number

ρ = Air Density (kg/m^3)

V = Air Velocity

D = Hydraulic Diameter (m)

μ = Kinematic Viscosity of Air (kg/m-s)

Since the flow in the channel is much too slow to be considered turbulent, equation 9 is used to find the coinciding friction factor with the Reynold's Number calculated.

$$f = \frac{64}{Re} \qquad \text{Eq. 10}$$

Where:

f = Friction Factor

Re = Reynold's Number

Equation 10 was used to find the experimental friction factor that was found during the calibration testing. This equation can also be seen on the Moody chart in accordance with the Darcy-Weissbach equation.

$$f = \frac{2PD_h}{L\rho V^2} \qquad \text{eq. 11}$$

Where:

f = Friction Factor

P = Pressure (Pa)

D_h = Hydraulic Diameter

L = Length Between Pressure Ports

ρ = Air Density

V = Air Velocity

Performing the friction factor testing was very simple as it only required a few data points at different flow rates to mimic the laminar flow section of the Moody Diagram. For each air flow velocity, a pressure measurement would be noted. Using those two pieces of information, the theoretical and experimental friction factors were found using the equations noted above. The results of these calculations were then plotted to see the validity of the numbers. After multiple runs and similar plots, it was deemed that the test section was sealed enough and ready for use. Figure 20 shows a Theoretical Friction Factor vs. Experimental Friction Factor for comparison.

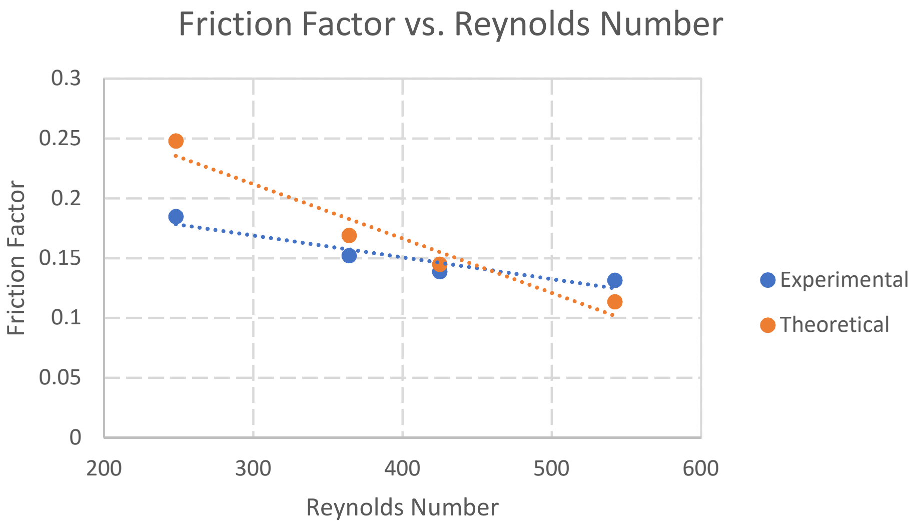

Figure 20: Friction Factor vs. Reynolds Number Results

Each Reynolds number has two corresponding points, a theoretical and an expected friction factor. This is because the velocity of the air is the only factor that changes the Reynolds number whereas there are two different sets of equations for finding the friction factor. One way is to use the Reynolds number and find the theoretical, while the other is to utilize the pressure taken and calculate the friction factor using that as shown in the equations previously noted. This plot proves that there is no loss in the test section, and therefore, it is fit to be used for further tests that include water.

Pressure to Flow Rate Conversion

After running a series of tests attempting to detach the water droplet from the floor of the test section, it was determined that the cap of 2000 mL/min that the flow meter was allotting was not enough for moving the droplet. It was determined that the flow meter should be removed from the final test setup to allow higher velocities to travel through the test section. It was determined that the best course of action would be to find the relationship between pressure and air flow velocity within the test section. This resulted in a linear plot shown in Figure 21. The resulting equation would govern all conversions from pressure to air flow rate velocity. This was also more accurate than using the flow meter, because the air flow measurements were coming from within the test section. There had been reports of loss in velocity between the flow meter and the test section through the speaker.

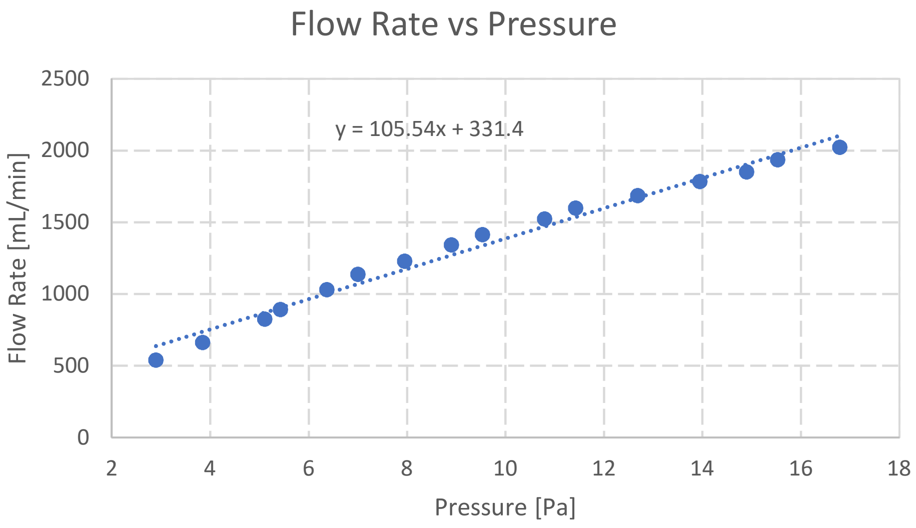

Figure 21: Pressure to Air Flow Rate Conversion Plot

Water Injection Tests

The final set of tests in this study introduce the two-phase flow aspect to the research. This test required the injection of water to channel while air is already flowing to simulate the conditions of a fuel cell. Different air and water flow rates were qualitatively tested before the optimal combination of the two was settled upon. This combination consisted of 6000 mL/min (7.81 m/s) of air and 60 µL/min (1 µL/s) of water. The combination of the two allowed for the best visualization of the droplets using the high-speed camera.

First, the test section needed to be assembled in such a way that allows the section to sit in the same place on the test stand. Next, the syringe pump needed to be connected to the test section via the connection on the bottom. After the water portion is connected, the air tube needed to be inserted into air inlet. The pressure transducer was then set up with the high-pressure port tubing inserted into the middle tap, and the low-pressure port tubing inserted into the end tap. Next, the camera would be placed on the stand and connected to the computer. The camera would then need to be focused to the test section to assure that the pictures being taken are as crisp and as clear as possible. Once the image portion was set up, the air portion was next. The LabVIEW VI was to be run throughout the duration of this portion to ensure that the right air velocity (6000 mL/min) was going through the test section. Any adjustments that needed to be made to the velocity could be done so by using the fine-tuning knob on the air line. Once the desired air flow was achieved, the water could be injected. Using the adjustment buttons on the syringe pump, 60 μL/min was selected, and the start button was pressed. When the first droplet began to grow, the record button on the Motion Studio software was pressed and the pictures began to take. After the recording was finished, the LabVIEW VI was turned off. Next, the water and air were switched off. All pieces that were connected to the test section were then disconnected. Finally, the test section needed to be taken apart to allow all the components to dry before the next test.

After the recordings were finished, the images needed time to process. During this time the Microsoft Excel file that was created could be examined to determine whether the data was usable or not. All the data was plotted so that it could be analyzed in the future. Once the images finished processing and saving, they could then be analyzed and examined.

Results

Optimal Acoustic Frequency

After each test was conducted, the LabVIEW VI could be turned off, which lead to printing the results in an Excel spreadsheet to be analyzed. This immediately led to the data processing stage, which began with plotting all the points and tailoring the spreadsheet to show relevant data points. This meant cutting out the data at the beginning and the end of each session as this was where the startup and shutdown procedures occurred. The statistic used to measure the efficiency of the different frequencies utilized is the time from buildup to detachment. This is easily measured by taking the difference between the time at the peak pressure data point of the plot and the time at the previous minimum pressure data point. After performing several tests, the time to detachments for each test were averaged out. These results can be seen in Figure 22.

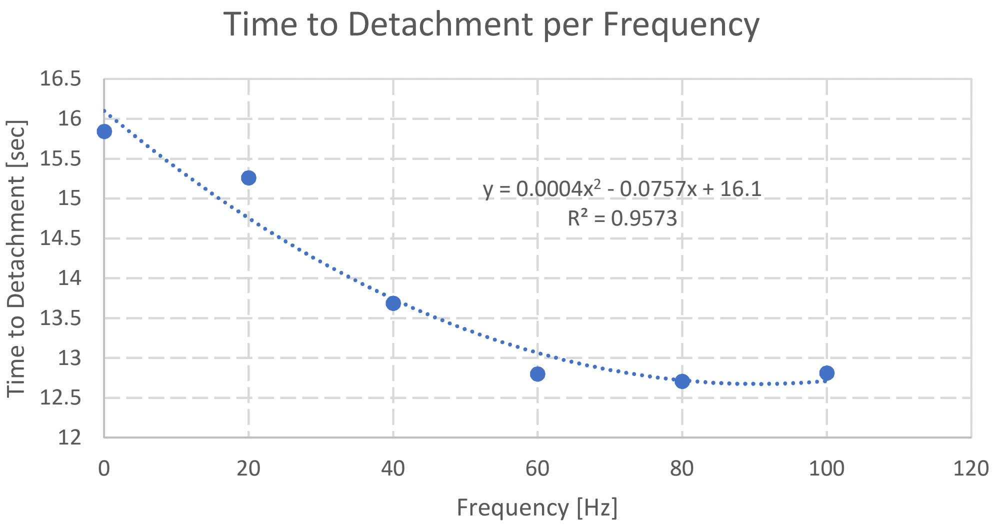

Figure 22: Time to Detachment Results

These results show that the most influential frequency in removing water is 80 Hz. The average time to detachment for the frequency of 80 Hz is 12.70 seconds. When compared to the 15.84 seconds the average at 0 Hz took, that is a 19.81% decrease in time. This is the largest percent decrease when compared with the other four frequencies. For 20 Hz, the average time was 15.26 seconds yielding a 3.69% decrease in time. 40 Hz tests averaged at 13.68 seconds, a 13.62% decrease. 60 Hz of frequency averaged 12.80 seconds, which results in 19.22% decrease in time. Finally, 100 Hz of added frequency to the air stream released the droplet at an average of 12.81 seconds, which yields a 19.15% decrease. This means that the natural frequency of the water entering a fuel cell is at, or near 80 Hz. Additionally, these results coincide with Mortazavi et al.'s discovery as noted previously in this essay. It was determined that 80 Hz had reduced the area of water by 85% when compared to 0 Hz [4]. This study gives an explanation as to why superimposing 80 Hz of frequency on the air supply within a fuel cell results in a lower cumulative water area. Less time between growth and detachment means that there is less time for the water droplet to grow.

Additionally, a difference in pressure study was done to understand more about the effects of superimposing a frequency on the air flow within a fuel cell. Understanding the different pressures at detachment is another indicator of how large the droplets grow to before they release. Figure 23 displays the difference in average pressure at detachment for each frequency.

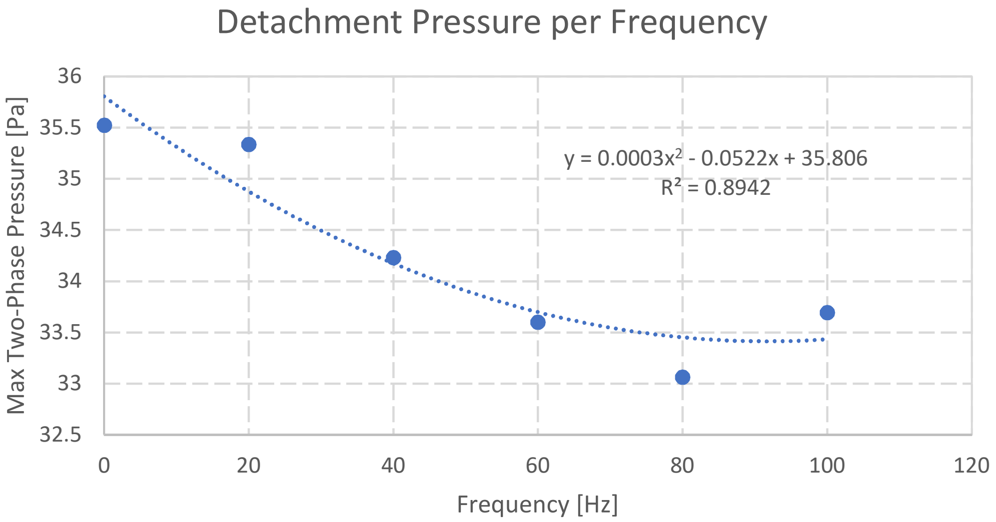

Figure 23: Detachment Pressure for Each Frequency

These results, yet again, prove that superimposing 80 Hz of frequency on to the air supply has the greatest impact on water droplets. The average maximum pressure at detachment for the 80 Hz trial was 33.06 Pa. Compared to the 35.52 Pa that was the maximum pressure at detachment for 0 Hz of imposed frequency, this yields a 6.93% decrease. The average detachment pressure for 20 Hz is 35.33 Pa, yielding a percent change of 0.53%. Superimposing 40 Hz of acoustic frequency on the air supply, the maximum pressure at detachment averaged out to 34.34 Pa, yielding a percent change of 3.64%. 60 Hz of acoustic wave superimposition resulted in an average detachment pressure of 33.6 Pa. This result returns a percent change of 5.42%. Finally, 100 Hz of superimposed acoustic frequency resulted in an average detachment pressure of 33.70 Pa, yielding a percent change of 5.16%. Like the time to detachment averages, this plot supports the fact that 80 Hz is the most efficient, while 60 Hz is the next most. This plot also shares the same shape as the time to detachment chart. 20 Hz of superimposed frequency does not do much, but there are sizable and noticeable decreases in pressure from 40 to 100 Hz.

The following images will display results for each case studied in this project. Each set of results displays the growth and detachment of multiple droplets. Those droplets follow the same growth cycle seen below. (1) First the water enters the channel which results in the droplet beginning to grow. (2) The pinned water droplet has grown enough in size that pressure and drag forces begin to change the shape of the droplet, which results in the lowered rise in pressure rate. (3) The net drag force on the droplet approaches the droplet's adhesion force to the surface and the droplet shakes uncontrollably. (4) Finally, the droplet has detached, and a new droplet begins to form following the same steps of the cycle.

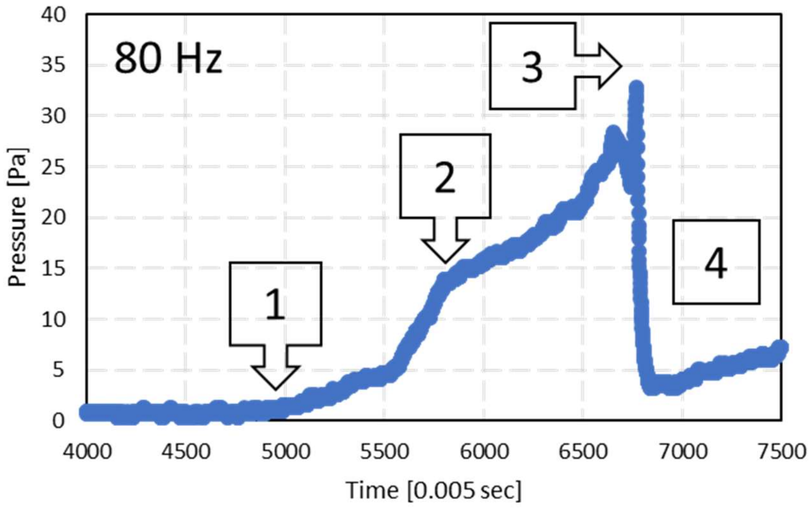

Figure 24: Single Cycle of Droplet Growth to Detachment

As noted earlier, the average time to detachment when 0 Hz of acoustic frequency is superimposed on the air supply is 15.84 seconds. This is the longest of any of the frequency trials. Additionally, the average pressure at detachment was 35.52 Pa. Figure 25 displays an overlaid comparison between all five superimposed acoustic pressure frequencies as well as the 0 Hz constant results. Each data set was overlaid on one plot to show the comparison between each data set. These sets, among others, can also be seen as separate plots in the Appendix.

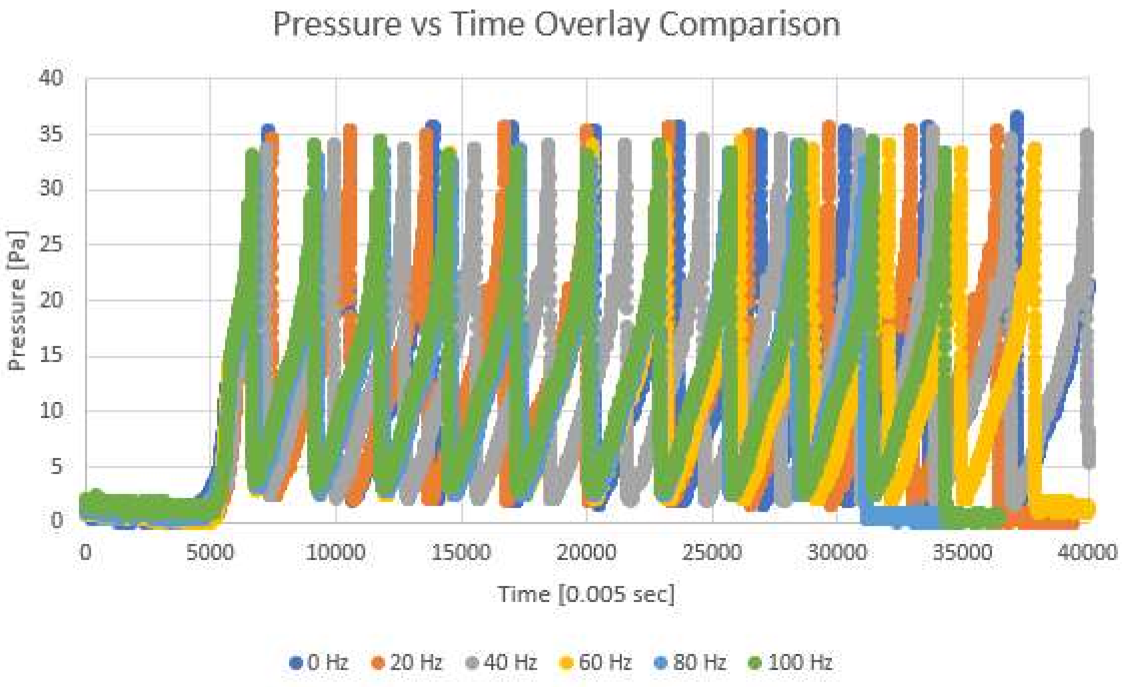

Figure 25: Pressure vs Time of all Six Trials

Each color of line is described in the legend. The darker blue line represents the data from the 0 Hz constant test. Each rise in pressure displays the growth of each water droplet and the drastic fall shows the droplet detaching and exiting the test section. Each of the droplets seem to have a small plateau before they reach the maximum size and detach. As more and more droplets grow and detach, that plateau seems to never go away and, in some cases, it is longer than the one before it. The last droplet recorded has the longest growth and the longest plateau. As a result, the largest pressure at detachment of 36.63 Pa is achieved. There were not any major discrepancies other than the one spike as most of the pressures seemed to stay around 35.37 Pa, which is the median detachment pressure for this trial.

The orange line represents the results from superimposing 20 Hz of sound waves on the air supply. In comparison to the 0 Hz plot, they both have the same initial buildup that includes a small decline in slope on the first droplet. Additionally, this test also includes the small plateaus that the 0 Hz test included. However, these are not as pronounced, which proves that even though the pressure does not change drastically, superimposing a frequency onto the air source will help immensely. The growth of the droplet does not get hindered. Additionally, all the pressures appear to be uniform throughout the test. The maximum pressure at detachment recorded during this test is 35.68. Additionally, the median detachment pressure is 35.37, like the 0 Hz trial. However, this median is not very far off from the maximum detachment, only 0.32 Pa, which proves the uniformity of the detachments. Additionally, the standard deviation of the data is 0.30 which validates the idea that this data set has the most consistent data. This is the lowest standard deviation of any of the data sets.

The grey line represents the 40 Hz trial. As with the first two sets of data shown, the first droplet had a noticeable drop in slope that it must overcome to reach that first peak. However, after the first droplet, every droplet after seemed to have no trouble at all making that maximum. The next difference to point out, is the plateau in the middle of the droplet growth is much less pronounced with the 40 Hz frequency when compared to the 20 and 0 Hz trials. Additionally, the median detachment pressure was 34.10 Pa, which is 1 Pa lower than that of the 20 Hz trial. However, the maximum detachment pressure is only 0.63 Pa lower than the 20 Hz set. Finally, the minimum pressure at detachment is 33.16 Pa. This set has the least consistent standard deviation at 0.62. This is also evident from the range between the maximum and the minimum being 1.90 Pa.

The 60 Hz result line is gold. After the first droplet, the plateau that has been showing up in past tests is not as clear in this trial, which means that the added frequency is actually helping smooth out the growth of the droplets. Each droplet growth seems to be identical to the one before it, which is a good sign that the 60 Hz of frequency is helping grow consistent droplets. The median pressure at detachment is 33.63 Pa. This is 0.79 Pa lower than the maximum pressure at detachment of 34.42. Additionally, the minimum detachment pressure is 32.84 Pa. Based on the appearance of the graph, the distribution of pressure seems to be very consistent throughout. The average time to detachment when superimposing 60 Hz of frequency on an air supply is 33.60 seconds. As it is evident from looking at the plot, this is not the most consistent detachment pressure. However, the pressures are still lower than the trials that precede it, so it is still more efficient at releasing liquid water droplets than 40, 20 and even 0 Hz.

The darker blue line represents the 80 Hz trial results. Even though this data set has the same buildup as the rest of the trials with regards to the first droplet, the shape of each buildup after is flawless. There is zero indication of plateaus, and this is great for saving time of the droplet growth. Hence, why the average time to detachment is 12.704 seconds, the quickest of each of the six tests. Additionally, the median pressure at detachment is 32.84 Pa. This is also the lowest of any of the six trials. The only concern with this set is the standard deviation being relatively higher at 0.57. However, this does not mean that it is not efficient, as the maximum detachment pressure is 34.10 Pa. Every statistic except for the standard deviation point to 80 Hz of superimposed frequency being the most efficient. This also proves that 80 Hz is at/or near the natural frequency of the droplets being grown in a PEM Fuel Cell.

Finally, the 100 Hz trial is represented by the green line. Although 100 Hz of frequency produces very similar buildup and detachment shapes as the 80 Hz trial, the time to detachments are a little bit higher. At 3.3% longer, it is not as effective at detaching water droplets as 80 Hz. However, droplets detached 19.15% faster than when no frequency is added. Additionally, the maximum droplet pressure at detachment is 34.32 Pa, and the median pressure is 33.79 Pa. Finally, the standard deviation is the second highest relative to the other six trials at 0.600. This is evident when looking at the plot as the different peaks create a sort of sine wave.

Additionally, the droplet volume at detachment was also calculated to understand the size of the droplets at detachment. This was calculated by taking the time interval between detachments and multiplying it with the injection rate of water into the test section. The complicated shape of the droplets makes it very difficult to measure the volume with accuracy, so this method allows for the closest estimation. After the analyzation of the data, it was found that 80 Hz of vibration reduced the droplet volume by around 20% compared to 0 Hz of vibration.

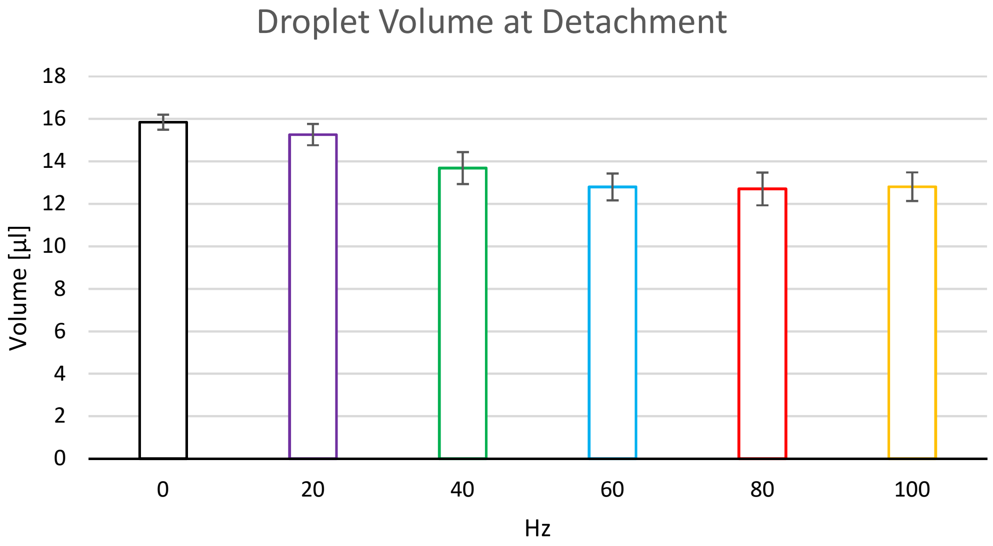

Figure 26: Comparing Droplet Detachment

Droplet Contact Angles

As noted in the procedure for this experiment, all the photographs were taken in the Motion Studio software. The purpose of these images is to qualitatively understand what the quantities in the data sets taken mean. Each individual picture taken corresponds to its respective data point, which allows for more insight on the subject. The purpose of taking these pictures was to understand how the droplets looks during growth and at detachment. Every set of numerical data has a corresponding set of images to go with it. This way any sort anomalies that occurred with the numerical set have an image that show the reason for that change. The data sets taken were 30 seconds worth of images at different frame rates. Different frame rates were needed for better detail with images. The frame rates are a function of the frequency that is superimposed on the air flow input. Unfortunately, the MotionPro Studio did not allow any longer than 30 seconds worth of images.

As noted in the previous section, the images are synchronized with the pressure data points taken. The two were able to be synchronized using the clocks on each of the computers. Each clock needed to be set using the Microsoft Internet clock. This ensured that the two clocks were synchronized down to the millisecond, which could then be used to analyze the data. From the images taken, videos of the process could be taken, as well as the use of these images to synthesize qualitative and quantitative data. Figure 27 displays the same Figure 20 shown in the previous section but with the corresponding images that were taken with the high-speed camera. The first image corresponds to the water entering the channel and the droplet beginning to form, this is shown in the pressure graph by the pressure beginning to rise. Next, the water droplet grows to a big enough size where the air impacts the physical shape of it, and it begins to deform in the direction of the air stream. Then the droplet has grown enough to detach from the aperture where the water enters and exit the channel. Finally, a new droplet has grown to replace the previous droplet, and the cycle starts over. The images shown in Figure 27 are taken from an 80 Hz trial that best exemplifies each step in the process and how they correspond to the timing of the data points.

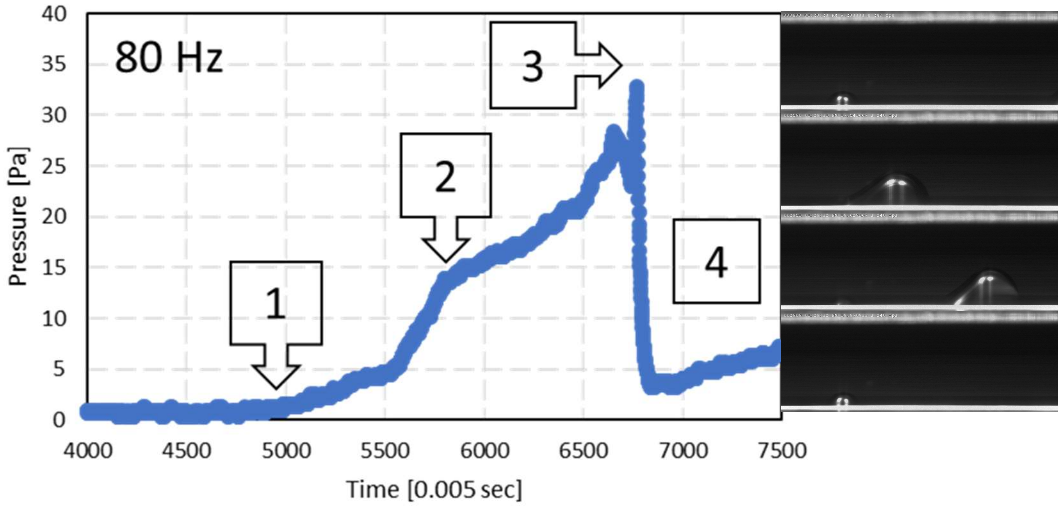

Figure 27: Graph with Corresponding Images

Along with the correspondence of images to the graph, the angle hysteresis could be taken using the images from the tests. The angle hysteresis of a liquid water droplet is characterized by two separate factors: the advancing and receding contact angles. Contact angle hysteresis is the difference between these two contacts. In each of the tests in this project, the advancing contact line always moved before the receding contact line. The images used for the purposes of this report were taken just before the droplet began moving down the channel. The reason for this is it is theorized that the larger the difference between the advancing and receding contact angles, the more unstable the droplet. This instability allows the droplet to detach much easier [6]. The image processing portion of this operation was done in AutoCAD 2019. From the image selected, the different contact angles could be outlined using the "Line" function in the program. The water droplet would act as a stencil, so the lines could be drawn on the image, itself, to allow for the most accurate angle measurements to be taken. A line was drawn at the base of the water droplet and the floor of the test section met. This line spans the length of the of that contact from the receding to the advancing tips. After drawing the base lines, the angle could be drawn using the endpoints on either side. An angle could then be formed by using the endpoint and drawing a line that outlined the droplet in the image. The angle measurements were taken using the "Angle" function in the program. All the angles taken from this portion of the experiment were compiled in a Microsoft Excel Workbook. 10 separate images were taken from each test run so that an average advancing and receding contact angle could be taken to account for human error. An example of an image used for processing is seen in Figure 28. This image was taken from an 80 Hz superimposed frequency run. Images that were too difficult to find the contact angles for any reason were omitted. This meant that the most accurate results could be taken by avoiding any guesswork that would cause even more human error.

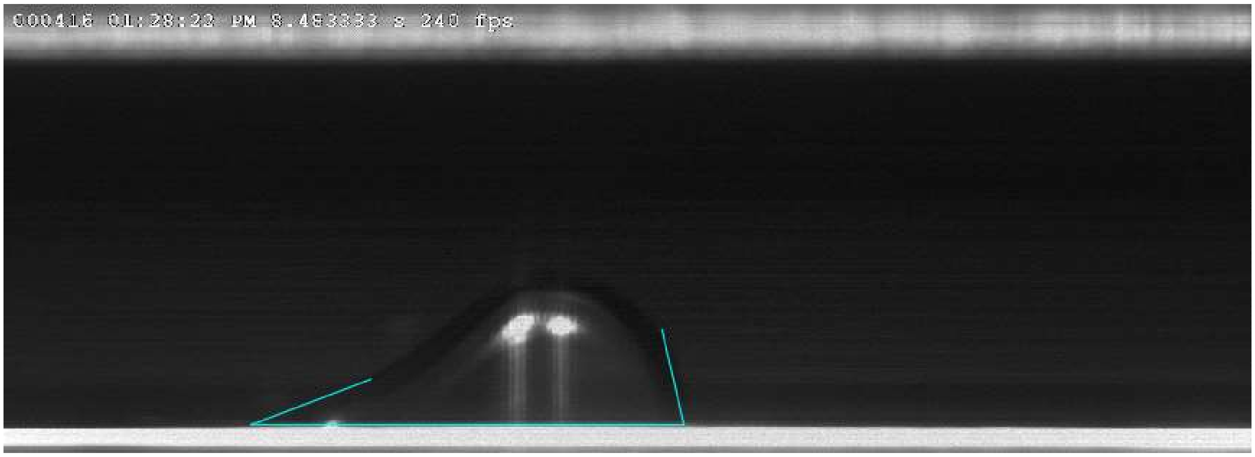

Figure 28: Image Processing Example

The results from this portion for the experiment are presented in Figure 29. This figure displays the differences in contact angles for all six different frequency cases run in this experiment.

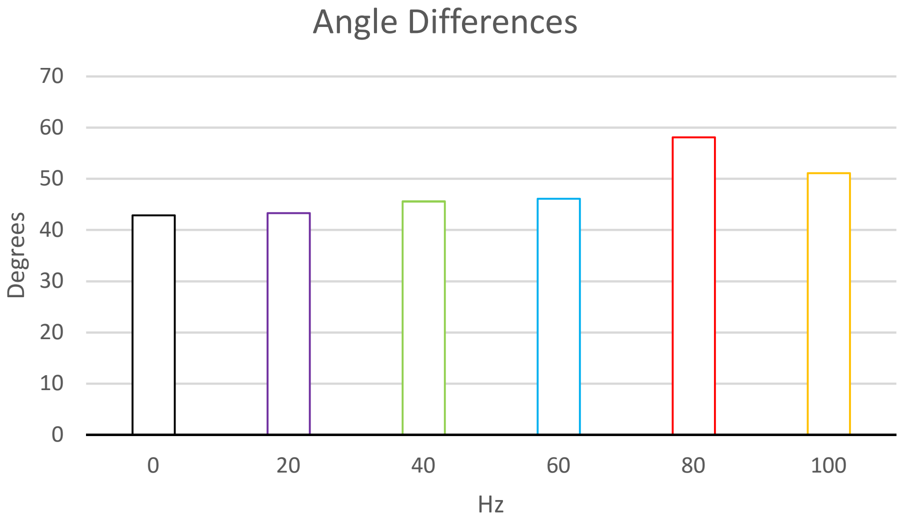

Figure 29: Contact Angle Differences

These results give their own explanation for why superimposing 80 Hz of frequency on the air stream is the most effective method for liquid water removal. If a curve were to be drawn on this figure, it would mirror the curve found in Figures 20 and 21. This continues the trend of an increase in efficiency from 0 to 80 Hz, however a decline occurs after 80 Hz. The difference of advancing and receding contact angles for 0 Hz is 42.88º. This same metric for 80 Hz is 58.1º which is a 35.6% increase in angle difference. That sizable change in angle difference is a glaring indicator as to why superimposing 80 Hz of frequency is so effective. Creating that large contact angle discrepancy causes more droplet instability, resulting in a much easier detachment process in less time. The next greatest increase was 100 Hz of frequency with 51.1º, yielding a 19.2% increase in angle difference. 40 and 60 Hz both had very similar angle differences at 45.6 and 46.1º, respectively. Finally, the 20 Hz of frequency only yielded a marginal increase of 0.42º, resulting in percent difference of 1%. This explains why the percent differences of the time and detachment pressures were much lower when compared to the other four frequency cases.

Droplet Oscillation

Qualitative notes were also made about the motion of the droplet while it was growing before detachment. Each of the frequencies used caused the droplet to oscillate or shake while growth was occurring. However, the oscillation and shape of the droplets would vary depending on the frequency used. The next six figures will be multiple image strings combined into one large image with the purpose of displaying the different oscillations of the water droplets with the different superimposed frequencies.

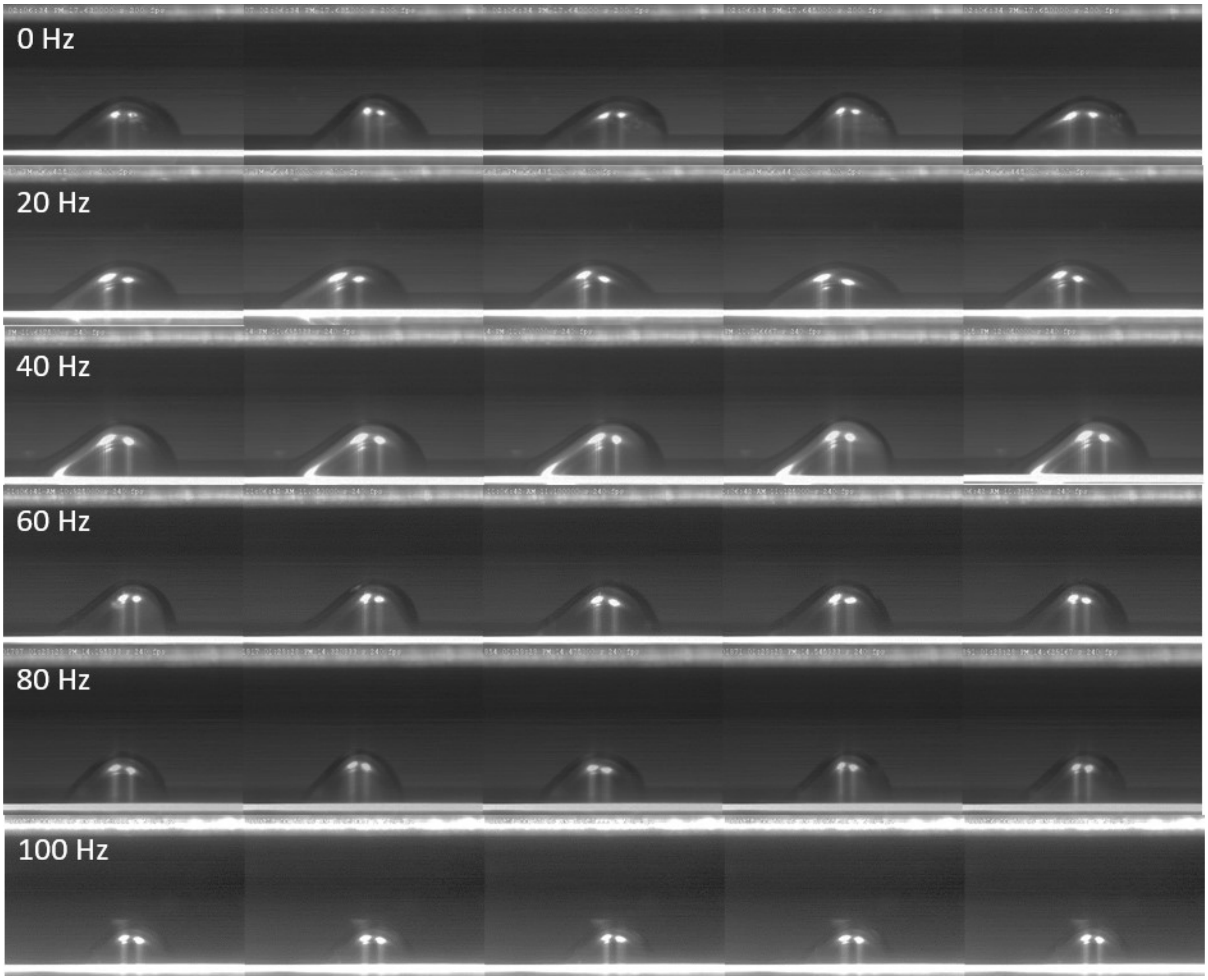

Figure 30: Droplet Oscillation with Various Frequencies

All the drag and oscillation are caused by air alone. There is no other external force that causes the movement of the droplet in this case. The motion of the droplet in this instance is more up and down as if the droplet is bouncing. At first, the droplet flattens out, before it returns to normal shape. This process occurs multiple times until droplet eventually shakes enough where it detaches and moves further down the test section toward the exit. The droplet detaches after the last image because at this point, the difference in contact angles is largest.

Adding 20 Hz of frequency to the air supply resulted in some very different looking droplet shapes. At first, the droplet takes on the typical shape seen in all other cases. However, after the droplet begins to oscillate, it begins to form a half circle. This is odd in that it is the only droplet set to exhibit this sort of behavior. After it forms the half circle, however, it does begin to form back into its regular forward moving shape before it propels down the test section. It can only be concluded that this small anomaly is helping force the droplet detachment. This testing case also happens to be the most pronounced change in droplet shape seen throughout the experiment.

After the 20 Hz frequency trial, the oscillation patterns for the droplets when impacted by 40, 60, and 100 Hz are all considerably uniform. The next set is the 40 Hz of frequency. To see the oscillation in these images, it is best to use the lighting as a guide. Noticing that the shadows on the righthand side of the droplet moves actually indicates that the droplet is shaking. Another key factor in this case is to notice that after the droplet goes through one full oscillation, it then lowers in height and the difference in contact angles grow. This can be noticed in the transition from the 4th to the 5th picture. The height of the droplet lowers, as a result, the receding contact angle lowers and the advancing contact angle greatens, causing a large difference between the two, propelling the droplet forward.

Next, 60 Hz was added to the air stream. This oscillation yielded similar looking results to adding 40 Hz of frequency in that the droplets did not necessarily change shape a large amount. However, noticing the lighting and shadows formed on the droplets, themselves, the droplet clearly oscillates forward and backward, rather than up and down. The middle most picture describes the largest oscillation movement from the rest of the shots because the advancing contact angle becomes comparably smaller. After that, however, the droplet returns to the typical look, and it soon detaches.

As probably anticipated, 80 Hz of superimposed frequency yielded the most change in shape throughout the growth and detach process. The addition of 80 Hz exhibited a much different oscillation than the rest of the cases. This case saw a up and down oscillation as well as a right to left all combined into one. Looking through the progression, it can be seen that the droplet starts lower, and left. By the second image, it shifts upward and more to the right. Image 3 sees a shift downward and even further right. Then in the fourth image, it shakes back up and to the left. Finally, the droplet regains its original shape before detaching. This is the most pronounced case of oscillations of any of the different frequencies utilized throughout the duration of this experiment.

The introduction of 100 Hz of frequency to the removal of water from the test section did not see a major change in the shape of the water droplet. Unlike the 80 Hz trials that saw a large shift in the outline of the droplet, the changes that occurred with 100 Hz were much smaller. Capturing all the motion required the brightness needed to be turned up on the camera because the shifts in position were so small. However, as small as the motion is that can be seen in these images, it is constant. The droplet's body never stops oscillating in all directions. Additionally, the droplet is lower in height than the rest of the cases tested. The height of the droplet never shifts up or down, however its peak is lower when compared to the other frequency trials.

Conclusions

Ex-Situ Test

The main goal of this project was to understand the effects of superimposing different frequencies on an air supply for the purposes of liquid water removal in a PEM fuel cell. A four-piece ex-situ test design was manufactured and assembled for the purpose of simulating the Cathode side of a fuel cell. Additionally, a complex laboratory setup was created that would allow the injection of an air stream with the superimposition of an acoustic frequency, while also making sure that frequency was not lost before the air reached the test section. Other parts of this test setup included the injection of water into the test section while also being able to take data points and run a high-speed camera for the purposes of analyzing pressure data against images of the water droplet going through the growth and detachment process.

Five different frequencies were added to a constant velocity air stream. Additionally, a test constant at 0 Hz was used for comparison purposes and to simulate the current method for water removal of fuel cells. The theory behind this project is to find the closest number to the natural frequency of the droplet because it would allow for the smallest droplet to detach in the quickest and most concise manner. A few different statistics were able to be tracked using the pressure and time data that was taken in a LabVIEW VI created for the specific purpose of this project.

After analyzing the quantitative results of the experiment, it can be concluded that superimposing 80 Hz of frequency on to the air supply is able to decrease the time from growth to detachment of the droplet by almost detachment by almost 20%. Additionally, the use of this same frequency was also able decrease the size of the droplet at detachment by almost 7%. This size difference may not seem like a lot, but this actually equates to about a 2.5 pascal decrease in maximum two-phase pressure. That result means that more droplets are able to detach and exit the fuel cell faster and with less effort.

Image Processing

The second goal of this project was to integrate a high-speed camera into the effort of synchronization with numerical data taken on a separate computer. Not only was this a complete success, but the data found was able to give explanations as to how and why 80 Hz was the most effective frequency that was superimposed onto the air stream. A qualitative and quantitative measure allowed for these explanations. One of these measures utilized taking the difference between the advancing and receding contact angles. It was said that the greater the difference between these contact angles, then it would be easier for the droplet to detach. The qualitative measure was to look at the images in order to understand the different how different frequencies can impact the shape of the droplet before detachment.

According to the images that were taken, this is because the difference in contact angles was largest for that frequency. This is because the difference in contact angles was 35.6% greater than when only air was injected into the space. Additionally, analyzing the images sequentially described that the droplets were most unstable when under the duress of 80 Hz superimposed onto the air stream. This was seen when closely looking at the shape of the water droplets as they grew to detachment. However, the droplets in the 80 Hz trials were noticeably altered at first glance. The work done with coordinating the timer on the high-speed camera with the timer on the LabVIEW VI will be able to be used in future projects that require this level of synchronization.

Recommendations Future Work

GDL

In the future, it is recommended that running these same exact tests utilizing factory made GDLs. Using an in-house treated GDL seemed to be problematic because the grain makeup of the microfibers was more random. This would cause issues when running tests because sometimes the grain would push the water into the walls of the test section and all the results from those tests would be void and unusable. Additionally, the GDLs used needed a lot of attention and care to ensure that they could be used again in future tests. This made it difficult to run a relatively short test multiple times because the test section would need to be disassembled and reassembled to run the next trial. Instead, professionally made and treated GDLs should be used in the future to ensure that the surface used is more conducive to the transport of liquid water. Professionally treated GDLs should alleviate all the problems mentioned and should yield more clean sets of results that can be used in reports.

High-Speed Camera

Additionally, although the camera and its software were extremely useful in taking quality pictures, it would be better if more computers on campus had the Motion Studio software downloaded to their hard drives and a second high-speed camera was purchased. A lot of waiting occurred because there is only one camera that can take images at the rates necessary for this experiment. Multiple different experiments were occurring on campus while also needed to utilize this camera. This meant that a lot of extra coordination and a lot of handoffs needed to occur with other students and professors. Having a second camera and multiple computers with the software would make accommodating the different schedules a lot easier.

Acoustic Wave Improvement

The next recommendation to be made is that a better method for the superimposition of the acoustic wave into the air supply. This may require some extra research, but there was always air loss through the speaker which caused the velocities in the test section change. To combat this issue, the velocity in the test section was directly correlated to the pressure measurement that was being taken. This ensured that the velocity being taken was in the section and not outside of the section as the previous design had called for using the flowmeter. However, the loss through the speaker also meant that more air needed to be pumped into the test section to reach the desired velocity. The extra air needed would deplete the air in the tank much quicker, and more would need to be ordered. Finding a better way to introduce the acoustic wave to the air stream would save air and allow for more certainty within the tests themselves.

In-Situ

The final recommendation for future work is to hopefully find a way to implement this same exact experiment but in-situ. Obviously, the end goal of the research is to find the best way to remove liquid water from a PEM fuel cell as to increase efficiency and further attempt to solidify fuel cells as a main source of power in the future. After understanding that superimposing acoustic waves into the air supply of a simple ex-situ design does remove water more efficiently, finding a way to carry this same method out in an in-situ test design could lead to better methods for water removal in the future.

References

[1] O' Hayre, Ryan. “Fuel Cells for Electrochemical Energy Conversion.” ResearchGate, Jan. 2017, www.researchgate.net/figure/Combined-fuel-cell-i-V-and-power-density-curves-The-power-density-curve-is-constructed_fig7_318669013.

[2] Zhang, F. Y., X. G. Yang, and C. Y. Wang. "Liquid Water Removal from a Polymer Electrolyte Fuel Cell." Journal of The Electrochemical Society 153.2 (2006): n. pag. Print.

[3] Palan, Vikrant, W. Steve Shepard, and Keith A. Williams. "Removal of Excess Product Water in a PEM Fuel Cell Stack by Vibrational and Acoustical Methods." *Journal of Power Sources*161.2 (2006): 1116-125. Print.

[4] Schafer, Andrew M., and Jeffrey S. Allen. "Improved Water Removal from Fuel Cell Flow Channels via Natural Frequency Excitation of Free Surfaces." *The Electrochemical Society*1887-1896 41.1 (2011): n. pag. Print.

[5] Mortazavi, Mehdi, Anthony D. Santamaria, Jingru Z. Benner, and Vedang Chauhan. "Enhanced Water Removal from PEM Fuel Cells Using Acoustic Pressure Waves." *Journal of The Electrochemical Society*166.7 (2019): n. pag. Print.

[6] Allen, J. S., S. Y. Son, and S. H. Collicott. *Proton Exchange Membrane Fuel Cell (PEMFC) Flow-field Design for Improved Water Management*. Diss. Michigan Tech, 2010. N.p.: Handbook of Fuel Cells - Fundamentals, Technology and Applications, 2010. Print.

[7] Bellis, Mary. "Hydrogen Fuel Cells Innovation for the 21st Century." *ThoughtCo*. ThoughtCo, 03 July 2019. Web. <https://www.thoughtco.com/hydrogen-fuel-cells-1991799>.

[8] "How Catalytic Converters Work." *HowStuffWorks*. N.p., 08 Nov. 2000. Web. 31 July 2019. <https://auto.howstuffworks.com/catalytic-converter1.htm>.

[9] "Nitrogen Oxide (NOx) Pollution." *Icopal Noxite A NOx Depolluting Roofing Membrane System*. N.p., n.d. Web. 31 July 2019. <http://www.icopal-noxite.co.uk/nox-problem/nox-pollution.aspx>.

[10] "Parts of a Fuel Cell." *Energy.gov*. N.p., n.d. Web. 31 July 2019. <https://www.energy.gov/eere/fuelcells/parts-fuel-cell>.

[11] Schafer, Andrew M. "A Technique for Improved Water Removal from PEM Fuel Cells via Natural Frequency Excitation of Free Surfaces." Diss. Michigan Technological U, 2010. Print.

[12] Mortazavi, Mehdi, et al. “Enhanced Liquid Water Removal from PEM Fuel Cell Flow Channels By Superimposing Acoustic Pressure Wave on Air Flow.” Proceedings of the 17th International Conference on Nanochannels & Microchannels and Minichannels, 2019

Appendix

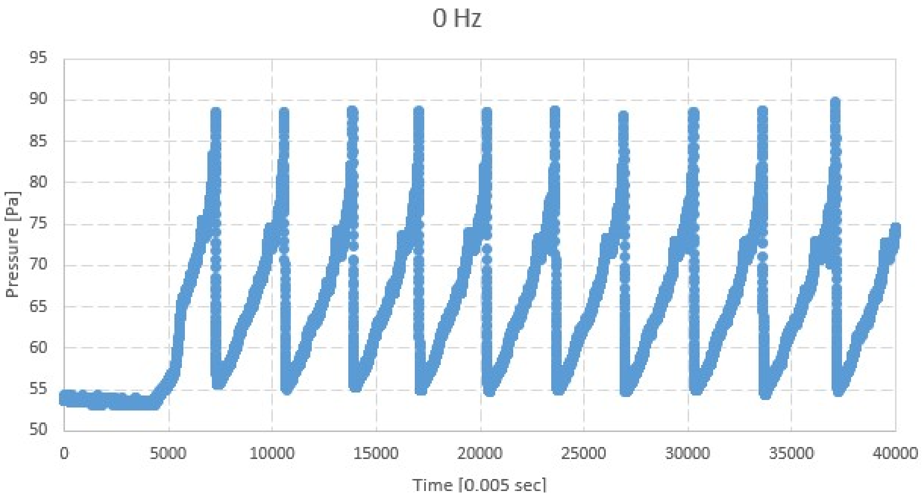

Figure A1: Pressure over Time 0 Hz

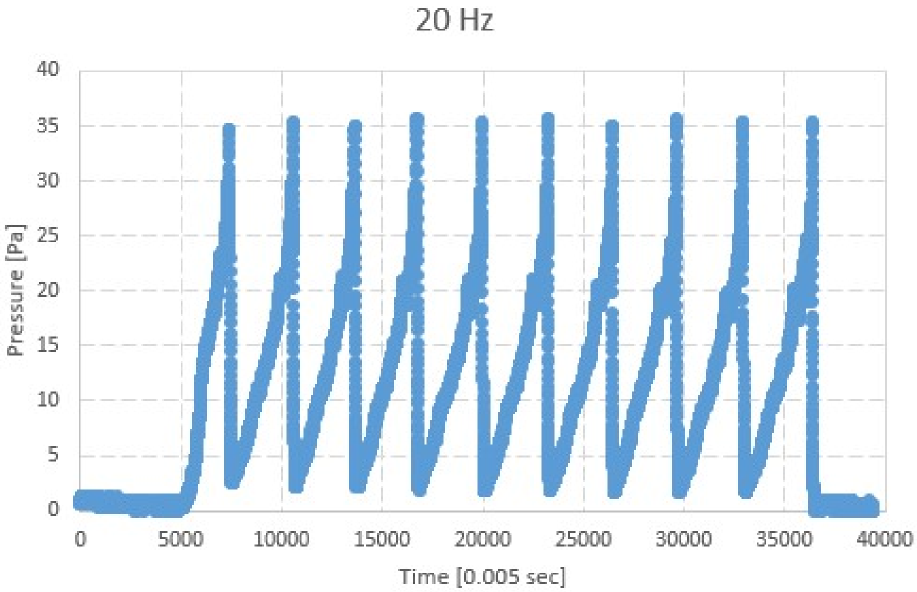

Figure A2: Pressure over Time 20 Hz

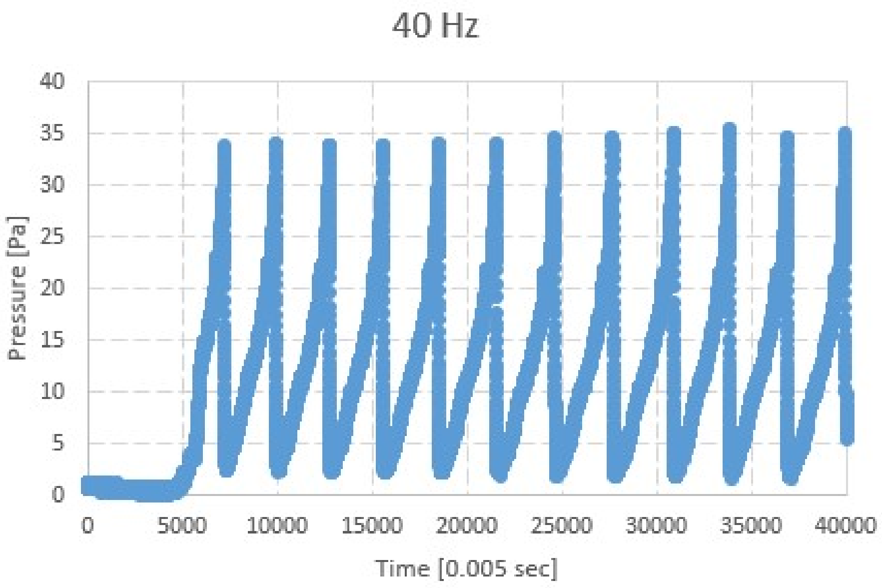

Figure A3: Pressure over Time 40 Hz

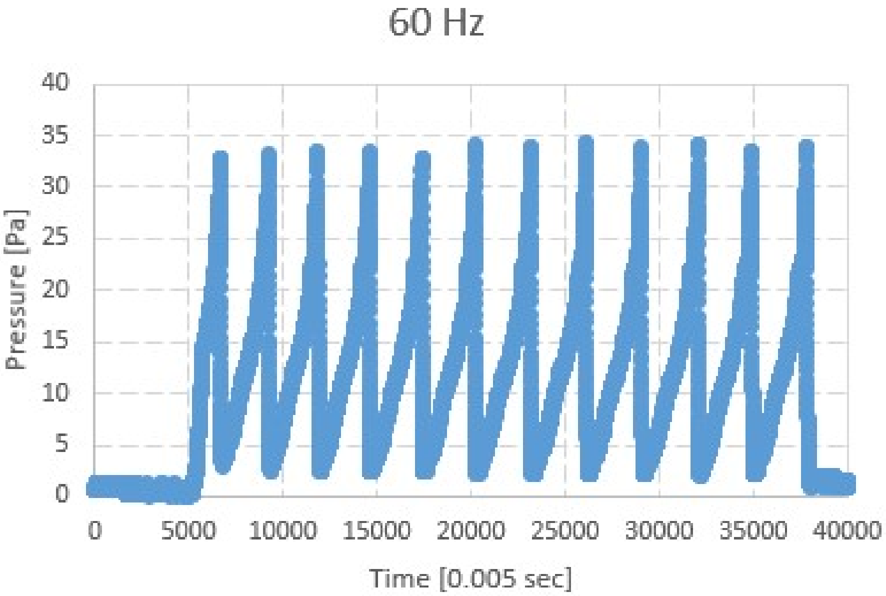

Figure A4: Pressure over Time 60 Hz

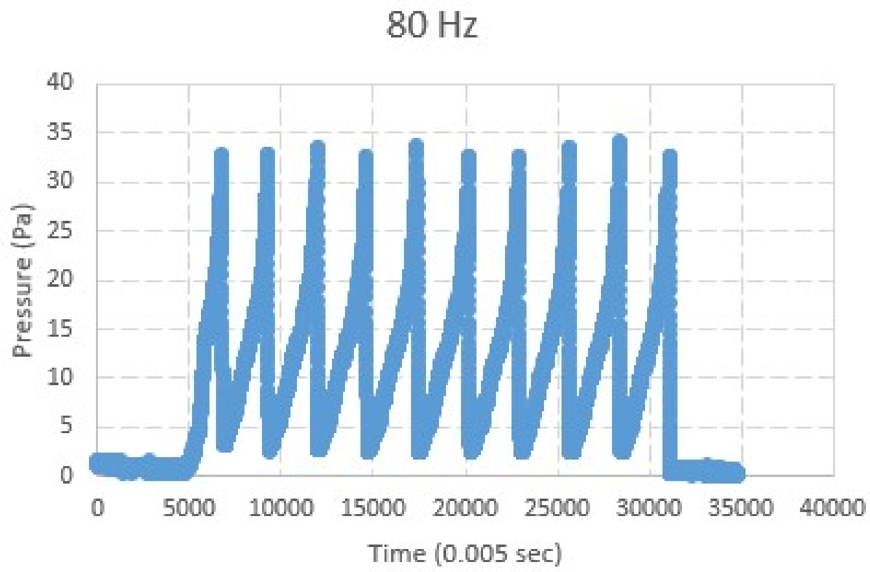

Figure A5: Pressure over Time 80 Hz

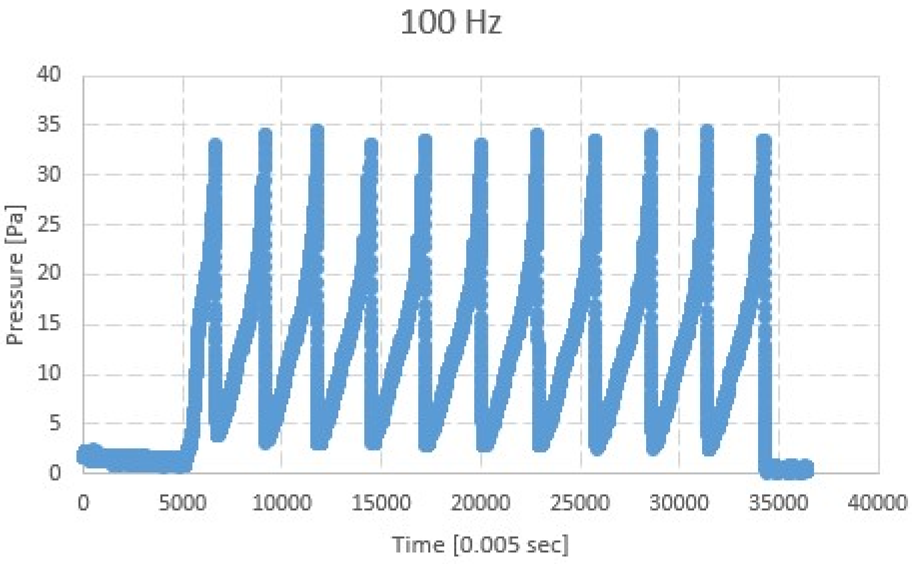

Figure A6: Pressure over Time 100 Hz